iScience

CellPress
OPEN ACCESS

Article

Location of the axon initial segment assembly can be predicted from neuronal shape

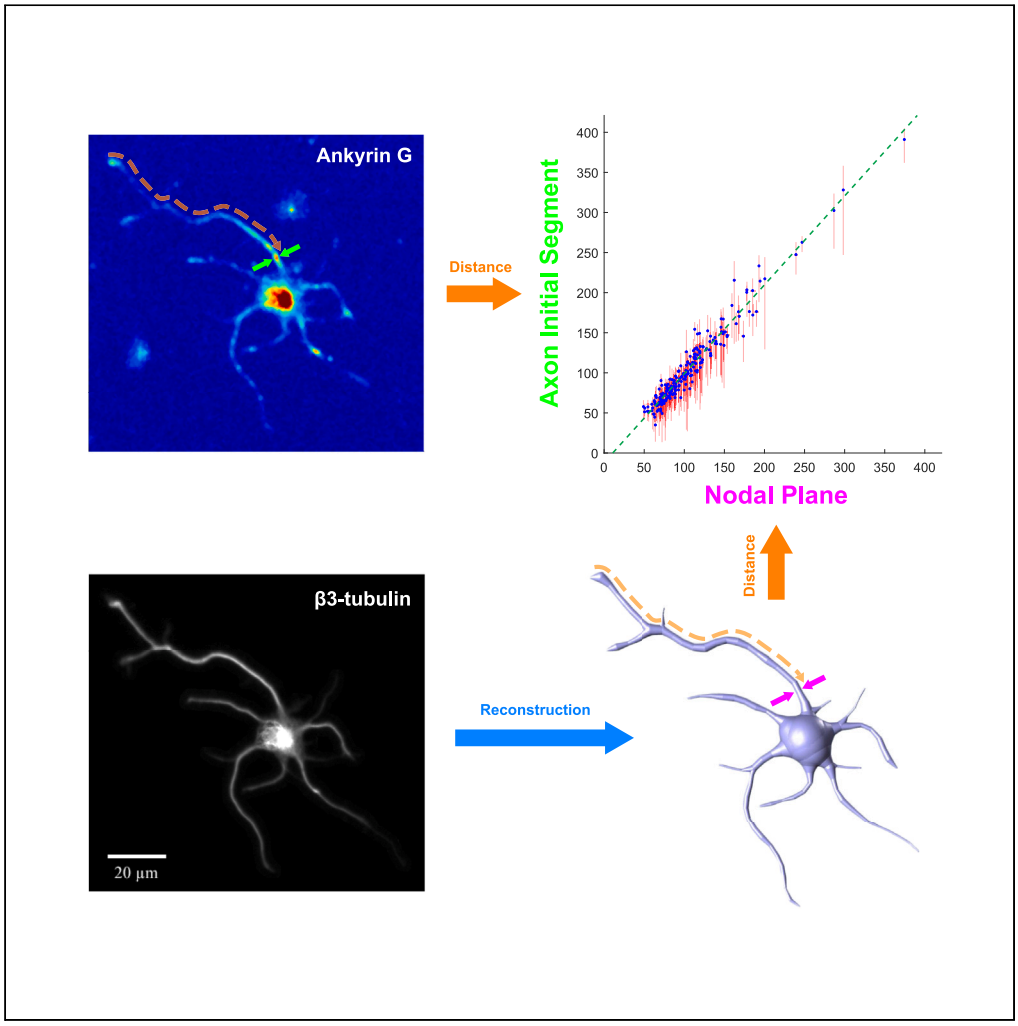

Zhuang Xu, Christopher N. Angstmann, Yuhuang Wu, Holly Stefen, Esmeralda Parić, Thomas Fath, Paul M.G. Curmi

p.curmi@unsw.edu.au

Highlights

Location of the AIS is correlated to cell shape of hippocampal neurons

AIS is located at the nodal plane of the lowest-order harmonic of the neuron shape

Correspondence between AIS and nodal plane is maintained in atypical neurons

Nodal plane exclusively locates on the Tau-enriched neurite

Xu et al., iScience 27, 109264
March 15, 2024
https://doi.org/10.1016/j.isci.2024.109264

iScience

CellPress
OPEN ACCESS

Article

Location of the axon initial segment assembly can be predicted from neuronal shape

Zhuang Xu,[1,2,3] Christopher N. Angstmann,[3] Yuhuang Wu,[4] Holly Stefen,[5] Esmeralda Parić,[5] Thomas Fath,[5] and Paul M.G. Curmi[1,2,6,*]

SUMMARY

The axon initial segment (AIS) is located at the proximal axon demarcating the boundary between axonal and somatodendritic compartments. The AIS facilitates the generation of action potentials and maintenance of neuronal polarity. In this study, we show that the location of AIS assembly, as marked by Ankyrin G, corresponds to the nodal plane of the lowest-order harmonic of the Laplace-Beltrami operator solved over the neuronal shape. This correlation establishes a coupling between location of AIS assembly and neuronal cell morphology. We validate this correlation for neurons with atypical morphology and neurons containing multiple AnkG clusters on distinct neurites, where the nodal plane selects the appropriate axon showing enriched Tau. Based on our findings, we propose that Turing patterning systems are candidates for dynamically governing AIS location. Overall, this study highlights the importance of neuronal cell morphology in determining the precise localization of the AIS within the proximal axon.

INTRODUCTION

Neurons are highly polarized cells featuring distinct axonal and somatodendritic compartments. The anatomical differences between these two major compartments are highlighted by a distinct protein composition and exclusive organelles present in each compartment. The axon-soma boundary is marked by a unique structural feature called the axon initial segment (AIS), which is usually 20–60 μm in length and located along the proximal axon in most neurons. The AIS is characterized by specific cytoskeletal adaptors, scaffold proteins, membrane adhesion molecules, and voltage-gated ion channels. It has two main roles in neuronal physiology: to maintain the high density of ion channels for efficient initiation of action potentials and to regulate the diffusion and differential trafficking of somatodendritic and axonal proteins, organelles, and vesicles for establishment and maintenance of neuronal polarity.[1] The proper assembly of the AIS is therefore vital for facilitating downstream signaling pathways that play a pivotal role in shaping the subsequent morphological development of neurons.[2–4]

In vitro studies have shown that the cultured embryonic hippocampal neurons are initially symmetric, with several non-differentiated neurites undergoing random extension and retraction. A symmetry-breaking process, known as axon specification, then transports a vast number of axon-specific proteins and organelles to a single neurite and drives its extension to become the nascent axon.[5,6] This is usually accompanied by the assembly of the AIS. Although the exact order of axon specification and AIS assembly remains to be unambiguously determined, the appearance of the AIS is generally thought to occur after axon specification.[7]

Banker and colleagues have shown that axon specification and AIS assembly in cultured mouse hippocampal neurons can be driven by cell-intrinsic mechanisms, obviating the requirement for external stimuli.[5,6] Experiments on axon regeneration after axotomy (axonal transection) demonstrate that neuronal polarity can be altered depending on the position of the transection site.[6,8–10] This suggests that axon specification during early neuronal development is capable of responding to morphological changes in neuronal cell shape. Furthermore, this dynamicity in axon specification is also observed in certain mature neurons.[11] Although the corresponding changes in the AIS during axon regeneration in these experiments have been characterized to a much lesser extent, recent *in vivo* experiments reveal that the AIS disassembles following axotomy, with the damaged multipolar neurons temporarily transiting to an immature state.[12] Additionally, a new AIS can re-assemble on the regenerated axon after a nerve crush.[13] From these results, one would expect that the dynamic responses to changes in neuronal cell geometry, as observed during axon regeneration, are also present in the *in vitro* assembly of the AIS.

Extensive efforts have been made to understand AIS assembly. One of the AIS scaffold proteins, Ankyrin G (AnkG), is often regarded as the master regulator of AIS assembly on account of its ability to interact with various components of the AIS scaffold, including the voltage-gated ion channels, the cell adhesion molecules (CAMs), and the cytoskeletal proteins, thereby stabilizing them within the scaffold.[12] Altering the

[1]School of Physics, The University of New South Wales, Sydney, NSW 2052, Australia
[2]School of Biotechnology and Biomolecular Sciences, The University of New South Wales, Sydney, NSW 2052, Australia
[3]School of Mathematics and Statistics, The University of New South Wales, Sydney, NSW 2052, Australia
[4]Infection Analytics Program, Kirby Institute for Infection and Immunity, The University of New South Wales, Sydney, NSW 2052, Australia
[5]Dementia Research Centre, Macquarie Medical School, Faculty of Medicine, Health and Human Sciences, Macquarie University, Sydney, NSW 2109, Australia
[6]Lead contact
*Correspondence: p.curmi@unsw.edu.au
https://doi.org/10.1016/j.isci.2024.109264

regulation of this scaffold, such as by manipulating actin cytoskeleton regulators myosin II, tropomyosin Tpm3.1, and mDia1, in turn, impacts the proper organization of AnkG at the AIS.[14–16] While AnkG unquestionably plays a vital role in AIS assembly and stabilization, it is not solely sufficient for complete AIS assembly. There are two major factors that contribute to this process: (i) the interplays between AnkG and the distal axonal components, including the axonal actin/α2/β2-spectrin/Ankyrin B scaffold, which are established shortly after axon specification,[17] and (ii) its associated membrane partners that act as linkers between AnkG and the membrane, such as Na+ channels and neurofascin 186.[18–20] However, it is worth noting that the specific nature of the interplay between AnkG and the distal axonal components remains a subject of ongoing investigation.

A lingering question in the field revolves around the intrinsic intracellular mechanisms responsible for establishing and sustaining neuronal polarity, specifically, what determines the position of AIS assembly. Given the complex nature of intracellular transport in neurons, addressing these questions poses significant challenges. Numerous molecular mechanisms are likely to operate concurrently to robustly and redundantly control neuronal polarization and AIS localization.[21,22] Moreover, the establishment of intricate sorting mechanisms and the age-dependent modulation of protein regulation during neuronal maturation add further complexity.[23,24] An underlying patterning system must exist to define a stable region for AnkG membrane anchoring, possibly mediated by upregulating the selective endocytosis for some AnkG membrane partners in the somatodendritic compartment and the distal axon. This can be inferred from the fact that the voltage-gated sodium channels (Nav1.2) are recognized by an endocytotic pathway, which leads to a selective elimination of these ion channels outside the AIS during the dynamic phase of AIS formation.[25] This, together with the submembranous actin/α2/β2-spectrin/AnkB scaffold, could work cooperatively to robustly position the AIS assembly at the proximal axon: shortly after axon specification, the distal actin/α2/β2-spectrin/AnkB scaffold forms in the nascent axon by backfilling toward the cell body. When the front of this backward extension encounters the "stable AnkG anchoring region" defined by some unknown patterning system, it then initiates the AnkG scaffold assembly around this region. This process is subsequently followed by the recruitment of various membrane, scaffolding, and cytoskeletal proteins to the region through their interactions with AnkG. Once they are properly anchored in the AnkG scaffold, their diffusion, turnover, and endocytosis are limited,[26–29] which in turn stabilizes AnkG and reinforces the whole scaffold. This positive feedback then drives the proper assembly of the AIS and stabilizes it. It is essential for such a patterning system to dynamically sense the geometry of neuronal cells, considering that axon specification is a dynamic process.

The localization and timing of intracellular structures regulated by geometry-sensing patterning systems appear to be a common feature across various cell types in all three domains of life. One prominent example of such regulation occurs during cell division in certain bacterial and archaeal strains, as well as in eukaryotic yeast.[30–33] In these cases, the localization process is likely influenced by the geometric properties of the cells, which can be inferred via calculating the spatial harmonics of the cell shape (also known as the eigenfunctions of the Laplace-Beltrami operator).[33,34] This raised the question of whether a similar patterning system is involved in the localization and assembly of the AIS in neurons. To gain insight into the nature of the underlying patterning system in developing neurons, we examined whether there is a link between the geometric properties of developing neuronal cells and the positioning of the AIS, which is closely associated with neuronal polarization.

Here we show that the location of the AIS assembly in the developing mouse hippocampal neurons (~3–5 days *in vitro* or DIVs) can be predicted from the neuronal shape via harmonic analysis. We examined the location of the AnkG peak (a marker of the AIS location) and showed that it correlates with the nodal plane of the lowest-order harmonic (leading eigenfuntion) of the Laplace-Beltrami operator solved over the neuronal cell shape, as the nodal plane generally resides within the detected AnkG-rich region. In addition, we found that the nodal plane tends to be located closer to the soma than the AnkG peak, while this tendency is weakened in the longest neurons. Examination of unusual neurons further supports our observed correlation. Analysis of a neuron with an atypical morphology (resembles that of the pseudo-unipolar neurons), which is rarely observed in hippocampal neuron culture, showed that the nodal plane of the lowest-order harmonic correlates to the AIS assembly site, despite a significant shift of the entire AnkG-rich region toward the axon terminal. Additionally, analysis of neurons that contain multiple AnkG clusters on distinct neurites shows that the harmonic nodal plane selects the AnkG-containing neurite to which the axon marker (antibody against total Tau) colocalizes. This demonstrates the capability of the nodal plane to recognize the nascent axon from the other neurites. Our results narrow down the characteristics of the underlying mechanisms for axon specification (neuronal polarization) and AIS localization. To be compatible with our observations, the underlying patterning mechanisms must be capable of generating spatial information on a cellular scale while simultaneously showing a clear connection to the spatial harmonics of cell shape. Candidate mechanisms include Turing patterning systems[34,35] and membrane energy minimization systems.[36] Based on our findings, we discuss the implication of Turing patterning systems as potential candidates for AIS localization.

RESULTS

Geometric characterization and analysis of neuronal cell shape

To test whether the AIS assembly site of the developing hippocampal neurons is related to the geometric properties of the neuron shape, primary mouse hippocampal neuron cultures were fixed at 3 DIVs and 5 DIVs. After fixation, hippocampal neuron cultures were immunofluorescently labeled for the cytoskeletal protein β3-tubulin, the AIS marker AnkG, the nuclear DNA marker 4′,6-diamidino-2-phenylindole (DAPI), and additionally the axonal marker Tau as per the protocol.[37] Subsequently, the corresponding fluorescence images were acquired; see Figure S1 for a sample image. Automated image analysis was used to isolate individual neurons using the β3-tubulin fluorescence images. Automatic neuronal tracing based on the APP2 algorithm was employed to obtain digital reconstructions of the extracted neurons. The shape of each neuron was then used to calculate low-order spatial harmonic functions and to locate their respective nodal planes.

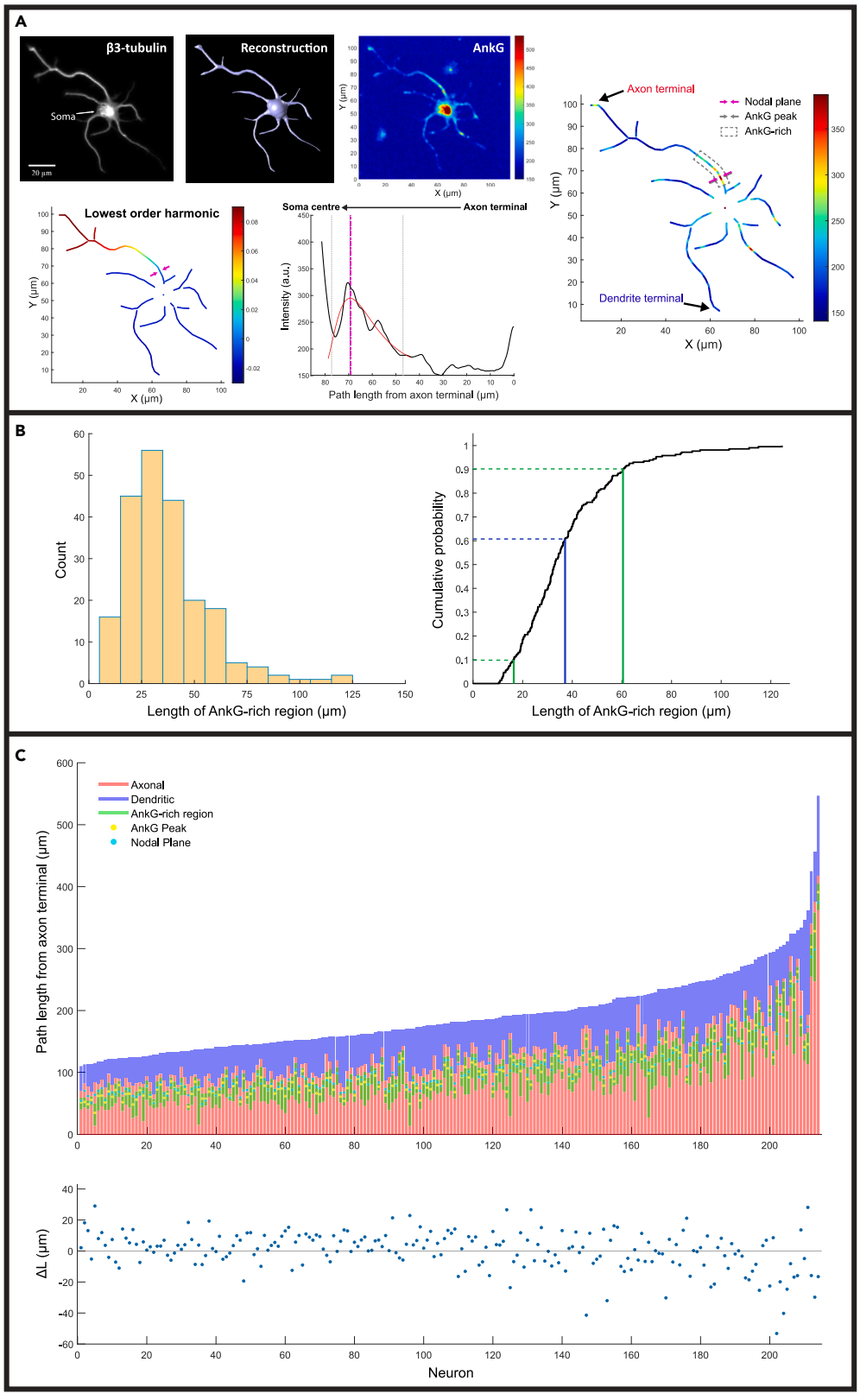
A
β3-tubulin
Soma
Reconstruction
AnkG
Axon terminal
Nodal plane
AnkG peak
AnkG-rich
Dendrite terminal
Lowest order harmonic
Soma centre
Axon terminal
Intensity (a.u.)
Path length from axon terminal (μm)
X (μm)
Y (μm)
B
Count
Length of AnkG-rich region (μm)
Cumulative probability
Length of AnkG-rich region (μm)
C
Axonal
Dendritic
AnkG-rich region
AnkG Peak
Nodal Plane
Path length from axon terminal (μm)
ΔL (μm)
Neuron

Figure 1. Overview of AIS assembly site analysis

(A) The workflow of the AIS localization analysis for a neuron. The filtered β3-tubulin fluorescence image of the neuron is used to generate the 3D reconstruction, from which the first few lowest-order harmonics and their nodal plane positions are determined (first image in the second row shows the lowest-order harmonic, nodal plane indicated by two opposite-facing magenta arrows). The plot of the smoothed AnkG intensity along the neurite on which the AnkG-rich region is identified as a function of path length measured from the axon terminal (solid black) is shown below the AnkG fluorescence image (AnkG intensity is saturated at the soma to enhance the contrast around the AIS) from which it is measured; the solid red line in the plot represents the fitted lognormal function around the AnkG peak; the locations of the estimated AnkG peak (lognormal function peak) and the nodal plane are indicated by the gray solid line and the magenta dash-dotted line, respectively, and the gray dotted lines show the boundaries of the AnkG-rich region based on the lognormal fit (positions where the fit reached 25% of the peak height). The rightmost image shows the AnkG fluorescence intensity evaluated on the traced neuronal skeleton, with the AnkG-rich region enclosed by the gray dashed box and the nodal plane of the lowest-order harmonic and estimated AnkG peak marked by the magenta and gray opposite-facing arrows, respectively (which almost perfectly colocalize in this case). The axon and dendrite terminals that are farthest from the estimated soma center are indicated by the arrows (useful in understanding the schematic results (C)).

(B) The length of the AnkG-rich region is defined as the full width at quarter maximum (FWQM) of the fitted lognormal function of the smoothed AnkG intensity. The histogram (left) shows all of the measured lengths for a total of 214 neurons identified with a clear AnkG-rich region. The right-hand plot shows the empirical cumulative distribution of the length of the AnkG-rich region, in which the 10th and the 90th percentile are indicated by green lines and the mean value is indicated by a blue line.

(C) Schematic representation of the relationship between the AIS peak and the nodal plane of the lowest-order harmonic for a total of 214 neurons analyzed. Features of individual neurons are plotted as a function of path length measured from the axon terminal on the y axis, in which the axonal and dendritic parts of the path are colored by red and blue, respectively. The boundary between red and blue bars hence indicates the position of the estimated soma center. The green section outlines the detected AnkG-rich region on the path, with the corresponding AnkG peak location marked by the yellow dot, while the nodal plane of the lowest-order harmonic is indicated by the cyan dot. The neurons are arranged in ascending order of the length of the longest neuronal path passing through the soma center and the axon and dendrite terminals. The corresponding signed path distances ΔL between the nodal plane of the lowest-order harmonic, and the AnkG peak for individual neurons are shown in the plot below. The sign of ΔL is defined such that a positive value would imply the estimated AnkG peak is closer to the axon terminal than the nodal plane (farther away from the soma).

To extract the AnkG peak location from the fluorescence image, a moving average filter with a width of 3–8 μm (depending on the noise level of the signal) was applied to the AnkG signal along the main axonal trunk to remove excessive noise. The smoothed signal was empirically fitted with a shifted lognormal function, from which the AnkG peak position and the length of the AnkG-rich region were estimated. It should be noted that the choice of the lognormal function is purely based on the skewness of the observed AnkG distributions; technically there is no biophysical model supporting the use of this functional form. An example of this workflow, from image analysis to nodal plane location, AnkG peak location, and AnkG-rich region detection, is illustrated in Figure 1A.

There are 35/214 cases where the observed AnkG distributions are not unimodal along the axon (Figure S2). Due to the limited pool of data, these cases were still included in our analysis in the following way: in the case of multiple closely spaced local AnkG peaks, the entire AnkG-rich region was fitted with the lognormal function; if the peaks were more spaced out, only the major peak closest to the soma was used for the fit. We note that in these less common cases, even though a clear AnkG-rich region can be identified, they lack a single well-defined peak, which might lead to poorly fitted lognormal functions.

The AIS represents a finite region separating the axon proper from the somatodendrite compartment. To estimate the length of the AIS, we defined the boundaries of the AnkG-rich region as the positions where the lognormal function reaches one-quarter of the maximum value at the AnkG peak. The length of the AnkG-rich region was then given by full width at quarter maximum (FWQM) of the lognormal function. The lengths of all measured AnkG-rich regions are shown as a histogram (Figure 1B, left), and the corresponding empirical cumulative function is also shown (Figure 1B, right). The mean of the AnkG-rich region length is 37.1 μm, with the 10th and 90th percentiles given by 16.4 μm and 60.4 μm, respectively. These values are in agreement with previous reports of the AIS being 10–60 μm in length.[38] The longer AIS beyond this range may be specific to the incipient AIS, as previous studies have shown that the length of the AIS decreases as the neuron matures (4 DIVs as opposed to 7 DIVs).[39] Thus, our AnkG detection method is consistent with previous work.

AIS assembly site correlated with geometric properties of the shape of the neuron, specifically, the nodal plane of the lowest-order harmonic

The location of the AnkG peak appears to be correlated to the position of the nodal plane of the lowest-order harmonic function of the cell shape. This can be seen in the visual representation (Figure 1C) of the AIS region for individual neurons (214 neurons in total), in which the features of the neuron are displayed along the longest neuronal path passing through the soma center and the axon and dendrite terminals. The positions of the AnkG peak and the nodal plane on this path are indicated by the yellow and cyan dots, respectively. The neurons are arranged in ascending order of neuronal path length. The path distance between the nodal plane of the lowest-order harmonic function of the neuronal cell shape and the AnkG peak (ΔL; Figure 1C lower scatterplot) provides an intuitive measure of the deviation between the experimental AnkG peak and the nodal plane of the lowest-order harmonic, so that a smaller value of this path distance generally implies a better correlation. The sign convention defines a positive sign as indicating a nodal plane distal to the axon terminal relative to the AnkG peak, and a negative sign as indicating a nodal plane proximal to the axon terminal.

One can see that the nodal planes correctly select the neurites on which the AnkG clusters are located for almost all of the multipolar neurons (Figure 1C, where the nodal plane lies on the axon usually within the AnkG-rich region). We identified three instances where the nodal plane does not lie on the neurite with the major AnkG cluster. However, in two of these cases, the nodal plane was found to be located on the

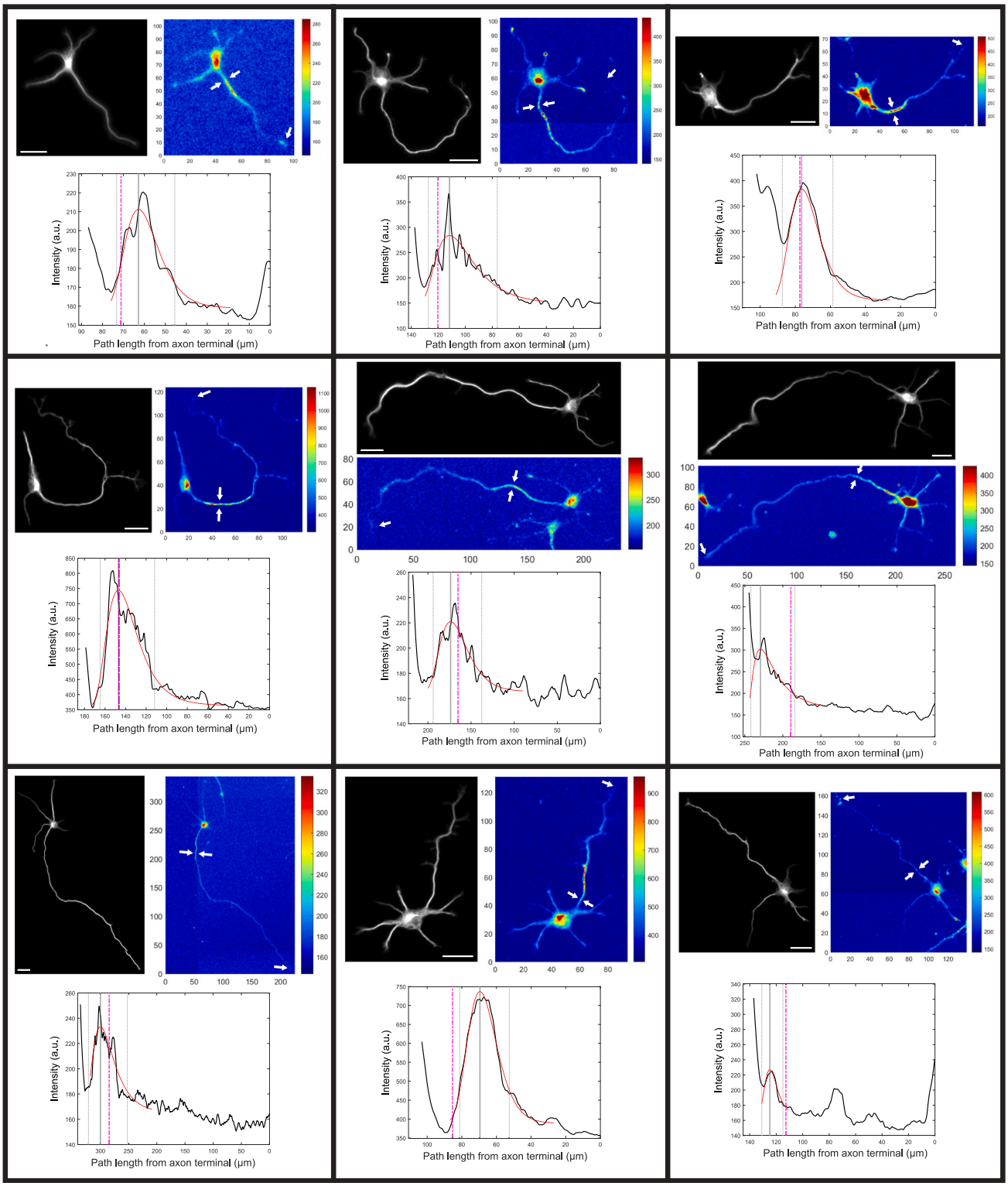

Figure 2. Representative examples of correlation between AIS and nodal plane positions

In each panel, the top two images show the filtered β3-tubulin fluorescence image of the isolated neuron (left) and the measured AnkG fluorescence intensity (right) (with the AnkG intensity saturated at the soma to enhance the contrast around the AIS). The bottom plot shows the smoothed AnkG intensity along the

Figure 2. *Continued*

neurite on which the AnkG-rich region is identified as a function of path length measured from the axon terminal (solid black curve where the origin is on the right). In each plot, the solid red line represents the fitted lognormal function around the AnkG peak with the locations of the estimated AnkG peak (lognormal function peak) and the nodal plane indicated by the gray vertical line and the magenta dash-dotted line, respectively, and the gray dotted lines showing the boundaries of the detected AnkG-rich region. Scale bar: 20 μm.

neurite that displayed a distally enriched Tau distribution (see Figure S3). In addition, approximately 80% of the neurons show a match between the AnkG peak position and the nodal plane of the lowest-order harmonic function, with the nodal planes lying within the AnkG-rich regions. We observe that the nodal plane lies within the detected AnkG-rich region in 79% (170/214) of the neurons; this percentage increases slightly to 82% (175/214) if the error estimate for the nodal plane position is taken into account (using a 20% increase/decrease in soma volume to test the robustness of our harmonic analysis, see supplemental information).

Representative examples of AnkG fluorescence images showing the location of the AIS along with the nodal plane of the lowest-order harmonic are provided in Figure 2. In each panel, the top two images show the β3-tubulin fluorescence image of the isolated neuron (note: the β3-tubulin images have been processed for automated neuron shape determination, see Figure S4) and the raw AnkG fluorescence image of individual neurons (nodal plane and axon terminal indicated by opposite-facing white arrows and a single white arrow, respectively). Note that the intensity of the AnkG fluorescence signal is truncated (saturated) in the region around the soma to enhance contrast and reveal the necessary level of detail around the AIS. The bottom image depicts the AnkG intensity along the developing axon, smoothed and plotted against the path length from the axon terminal. The plot includes the solid black line representing the measured AnkG intensity, as well as the fitted lognormal function shown by the solid red curve. Additional visual indicators are provided: the solid gray line indicates the position of the measured AnkG peak, the gray dotted lines represent the boundaries of the AnkG-rich region, and the magenta dash-dotted line corresponds to the nodal plane. Note that the origin of the path length (axon terminal) is on the right of each graph while the soma is at the intersection with the y axis.

In most cases, the nodal plane of the lowest-order harmonic function (magenta dot-dashed line) lies near the AnkG peak (gray line) and within the detected AnkG-rich region (between two gray dotted lines; see examples in Figure 2 with the exception of the last two examples, where the nodal plane is just outside the AnkG-rich region). We also observed a tendency of the nodal plane to be located closer to soma than the AnkG peak when neurons are small (see Figure 1C, residual plot), and vice versa when the neurons become larger. The localization patterns of the AnkG signal in early-developing neurons frequently exhibit a bias toward the axon terminal. However, the precise origin of this asymmetry and its biological implications remain elusive. Interestingly, AnkG was sometimes found enriched at certain neurite tips (see Figure 2, the top-left and bottom-right panels). No clear pattern was observed as to which neurons/neurites are associated with these terminal AnkG clusters.

Figure 3A shows a histogram of the signed path distance between the nodal planes of the lowest-order harmonic function of the neuron cell shape and the measured AnkG peak. It shows that, in general, the nodal planes are slightly closer to the soma than the measured AnkG peak (mode of ΔL +5 μm, mean + 0.41 μm, median +2.17 μm), with 66% of the neurons having an absolute deviation |ΔL| less than 10 μm and more than 90% of the neurons having a value within 0–20 μm. These deviations are small relative to the size of the neurons, where the deviations mostly vary within 10% of the neuronal path length (Figure S5). The corresponding quantile-quantile (QQ) plot of ΔL (Figure 3B) shows that its distribution is slightly left skewed (as can also be seen in the histogram in Figure 3A); this is likely caused by the tendency of the nodal plane to move toward the axon terminal for the longest neurons. The scatterplot (Figure 3C) shows that the positions of the AnkG peak and the nodal plane along the axon are highly correlated with the correlation between the variables estimated to be 0.97. In this plot, the terminal of the longest axon (see Figure 1C) is used as the reference point without loss of generality (Other boundary reference points such as the longest dendritic terminal could be used, but this would increase the noise level as the resulting path will go through the soma center whose position can only be estimated approximately, see Figure S5). The slope of the linear regression line of the data points is 1.11 ± 0.042 (SE of regression) with the y-intercept $-11.92 \pm 4.77 \mu m$.

To check whether the skewed distribution of the distance between the nodal plane and the AnkG peak, ΔL, is caused by the measurements on the longest neurons, a similar analysis was performed on neurons with neuronal path lengths less than 185 μm (118 neurons; Figures 3D–3F). This choice of maximum length was based on the observation that the ΔL becomes more scattered for neurons greater than 185 μm (see the residual plot of ΔL at the bottom of Figure 1C). We see that ΔL for these neurons with shorter neurites becomes almost normally distributed as the points fall near a straight line in the QQ-plot (Figure 3E), suggesting that the deviations may be attributed to random errors and approximations made during evaluation of the nodal plane and estimation of the AnkG peak. The distribution is centered at +3.98 μm; this implies that the nodal plane position along the axon, on average, is 3.98 μm closer to the soma than it is to the AnkG peak. This is also reflected by the downward shift of the linear regression line (Figure 3F) with the slope 1.00 ± 0.066 (SE of regression) and the y-intercept $-3.76 \pm 1.20 \mu m$. The slope of 1.00 ± 0.066 with a correlation coefficient of 0.87 provides strong evidence that the nodal plane and the AnkG peak are connected by some underlying phenomenon.

Colocalization of the AIS position and the nodal plane for multipolar neurons with a clear soma-AIS gap

The AIS usually starts near the soma boundary along the nascent axon, but sometimes it is more distally located. If this distal axonal shift in the AIS position is reflected in the corresponding position of the nodal plane of the lowest-order harmonic function, then this would provide stronger evidence for the correlation between the AIS position and the nodal plane, as opposed to both just being colocalized to the boundary of

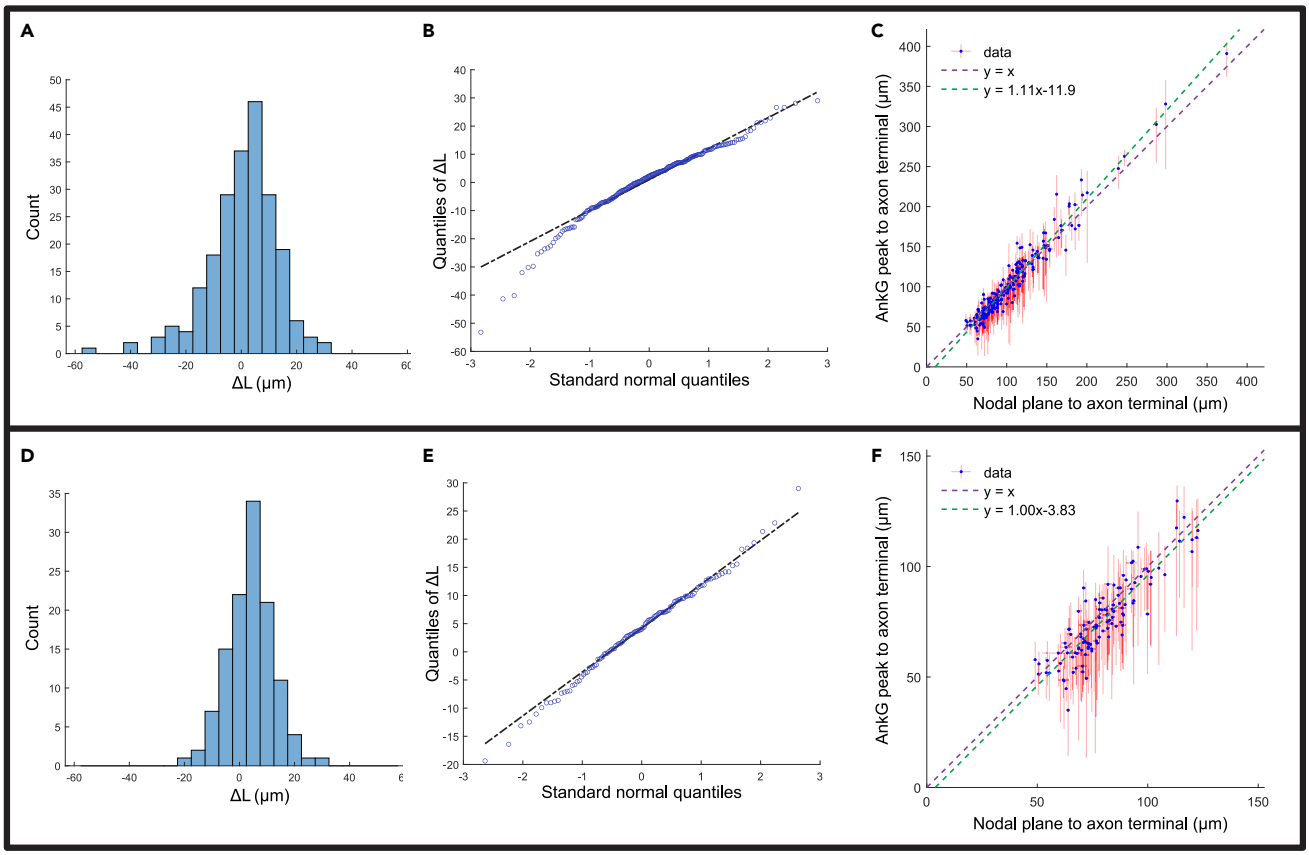

Figure 3. Analysis of correlation between AIS and nodal plane positions

(A) Histogram of the signed path distance between the nodal plane and AnkG peak, in which a positive value would imply that the nodal plane is closer to soma than the detected AnkG peak.

(B) Normal quantile-quantile (QQ) plot showing the observed quantiles of the signed path distance between the nodal plane and AnkG peak versus quantiles expected from a standard normal distribution. The black dot-dashed reference line indicates the expected quantiles distribution under the null hypothesis that the signed path distances follow a normal distribution.

(C) Scatterplot of the path distance from the axon terminal to the AnkG peak versus the path distance to the nodal plane for the 214 analyzed hippocampal neurons (3,5 DIV), with error bars drawn at each data point. The error bars in the x-direction are estimated from the shifts in nodal plane location calculated by increasing or decreasing soma volume by 20%, whereas the error bars in the y-direction are estimated from the path distance between the boundaries of the AnkG-rich region and the corresponding AnkG peak. In this way, the error bar above the data points represents the boundary of the AnkG-rich region closer to soma and the one below the points indicates the other boundary closer to the axon terminal. The purple dashed line plots the equation y = x so that difference in y-coordinate between the data points and the line gives the path distance between the nodal plane and AnkG peak. The green dashed line shows the linear regression line of the data points using the least-squares method.

(D–F) demonstrate the same analysis as (A–C) but only utilize data from the 118 neurons with a maximum neuronal path length less than 185 μm. (D) Histogram of ΔL for neurons with neuronal path length less than 185 μm. (E) Corresponding normal QQ-plot of ΔL against theoretical quantile values from a normal distribution, with the dot-dashed reference line shown in black. (F) Scatterplot of the path distance from the axon terminal to the AnkG peak versus the distance to the nodal plane for the 118 neurons with a neuronal path length of less than 185 μm.

the soma (start of the axonal branch). For the 214 neurons extracted from the mouse hippocampal neuron cultures, we identified five cases in which a relatively large soma-AIS gap was evident (Figure 4). The neurons isolated here are all multipolar and contain relatively flat AnkG-deficient regions approximately 20 μm in length, which are located just after the soma boundary (the position near the sharp drop in AnkG intensity shown near the left edge of the intensity versus path length graphs in Figure 4) and before the closest boundary of the AnkG cluster. The path distances between the soma boundary and the closest AnkG peak are at least 30 μm. As per our analysis, we calculated the position of the nodal plane of the lowest-order harmonic of the neuron shape and compared this to the detected AnkG peak. The examples of the neurons with abnormal distributions of AnkG are illustrated in the first column in Figure 4. In the top-left example, the AnkG-rich region consists of two closely spaced local peaks, while, in the bottom-left, three local peaks are seen on the nascent axon. Despite having less well-defined AnkG peaks, the position of the nodal plane in both examples is positioned right on the local AnkG maximum closest to the soma. In the other three examples, the nodal planes lie close to the AnkG peak and slightly closer to the somas, but within the detected AnkG-rich region. The results here are generally similar to those of most other neurons analyzed, where a match between the nodal plane

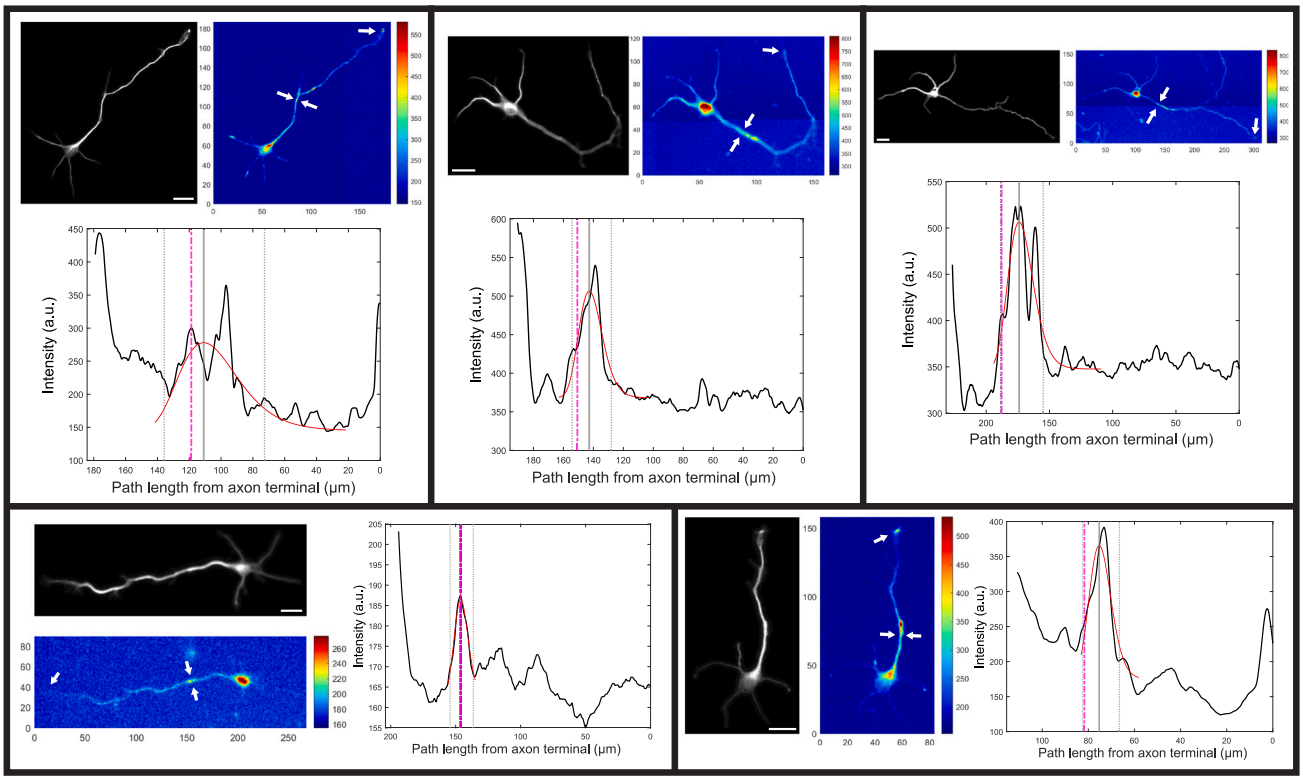

Figure 4. Colocalization of AIS and nodal plane in neurons exhibiting a clear soma-AIS gap

Each panel illustrates a neuron with a distinct soma-AIS gap.The top two images in each panel display the filtered β3-tubulin fluorescence image of the isolated neuron (black background) and the measured AnkG fluorescence intensity (blue background), with the AnkG intensity saturated at the soma to enhance the contrast around the AIS. The bottom plot depicts the smoothed AnkG intensity, featuring elements similar to those shown in Figure 2. Scale bar: 20 μm.

location and the AnkG peak is found with a tendency of the nodal plane to sit on the somal side of the AnkG-rich region. This suggests that the nodal plane of the harmonic is correlated to the AnkG position even when the neurons have relatively large soma-AIS gaps creating distally located AISs.

AIS localization in a hippocampal neuron with an atypical morphology

Our focus in this study is primarily on multipolar neurons, as they constitute the predominant population in our mouse hippocampal neuron culture. Intriguingly, a single neuron exhibiting an atypical morphology was identified within the neuron culture. This neuron possesses a unique and peculiar morphology characterized by a solitary axon originating from the soma, which bifurcates into two axonal branches, forming a T-junction. Note here the segment between the soma and the junction point is termed the "stem axon." Since harmonic analysis is dynamically responsive to cell shape, this difference in morphology is likely to induce some changes in the resulting nodal plane location. As such, the AIS in this neuron is expected to show signs that are distinct from those of the multipolar neurons.

Indeed, in the identified neuron with an atypical morphology, the AnkG-rich region is observed on the stem axon near the T-junction. Notably, both the peak position and the boundary of the AnkG-rich region are more distally located from the soma compared to those typically seen in multipolar neurons (Figure 5). The distal axonal side of the AnkG-rich region extends a short distance beyond the T-junction into the two axonal branches, while the previously observed skewness of the AnkG distribution is preserved (as seen in the lognormal fit in Figure 5E, red curve). This neuron with an atypical morphology thus serves as a comparative test for models predicting the position of the AIS based on neuron shape.

Interestingly, in this case, the AIS position determined by the AnkG peak still matches the position of the nodal plane of the lowest-order harmonic, which is only 7.2 μm away from the AnkG peak and lies within the AnkG-rich region. It is important to note that this difference is small compared to the length of the AnkG-rich region (44.2 μm) and even smaller when compared to the overall neuronal path length (223.5 μm).

In neurons containing multiple AnkG peaks on distinct neurites, the nodal plane selects the correct arbor for axonal specification

The distribution of AnkG in early-developing neurons can be diverse (3–5 DIVs) and does not always exhibit a singular well-defined peak. A notable scenario arises when AnkG clusters are observed at the proximal regions of distinct neurites within a single neuron. Of the 214

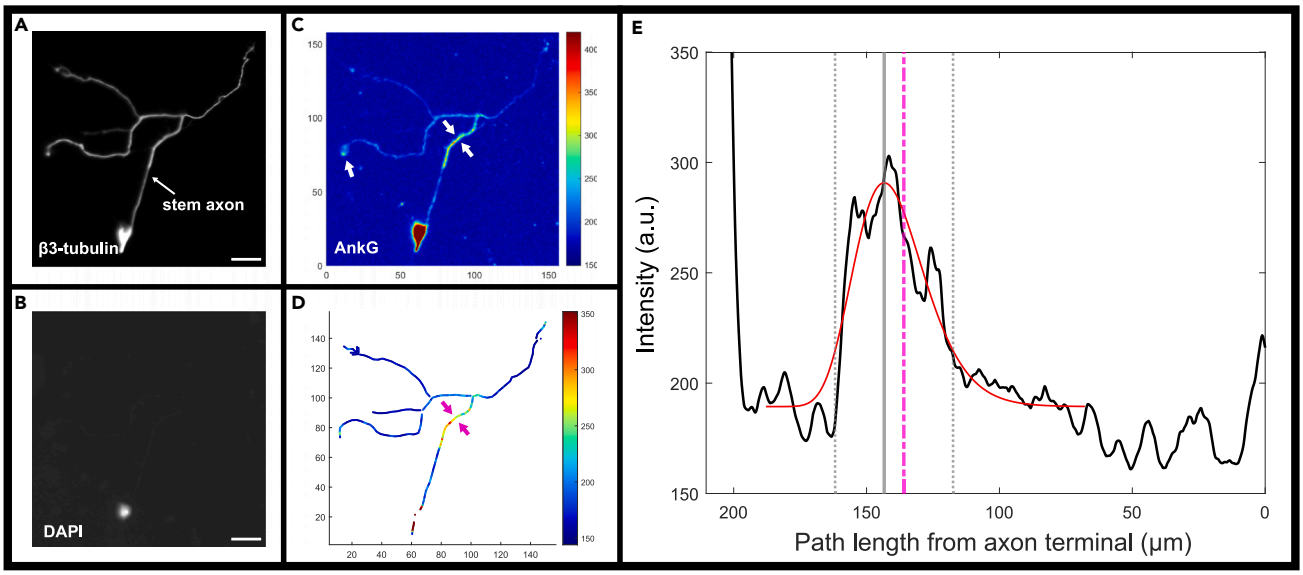

Figure 5. Colocalization of AIS and nodal plane in a neuron with an atypical morphology

(A) The filtered β3-tubulin fluorescence image marks the envelope of the neuron and the stem axon.

(B) The DAPI fluorescence image which stains the nucleus (bright spot) and identifies the location of the soma.

(C) The measured AnkG fluorescence, where the top 40% of high-intensity signals at the soma are saturated for better visualization of the AnkG-rich region.

(D) The AnkG fluorescence intensity evaluated on the traced neuronal skeleton, with the nodal plane of the lowest-order harmonic marked by two opposite-facing magenta arrows.

(E) The plot of the smoothed AnkG intensity along the nascent axon, with features plotted in the same way as those shown in Figure 2. Scale bar: 20 μm.

analyzed neurons, 6 neurons (approximately 3% of the total) were identified to contain two major AnkG clusters on two distinct neurites (Figure 6, AnkG clusters indicated by white arrowheads in the AnkG images), and both clusters could potentially become the AIS or even form multiple AISs in the future (we note that multiple AISs are usually observed under pathological conditions such as drug-induced actin depolarization or inhibition of GSK-3 beta activity[9,40,41]).

Despite having the AnkG clusters located on two distinct neurites, the axon-specific protein Tau was only found enriched in the distal region in one of the neurites (Figure 6, Tau fluorescence image in each panel). This suggests that only the AnkG cluster on the neurite with a distal enriched Tau distribution will become the AIS in the future (i.e., we assume that the polarized Tau distribution signifies the real "axon"), while the other cluster is likely to disappear as the neuron matures. Based on this assumption, these neurons with multiple AnkG peaks located on different neurites can serve to test the robustness of the correlation between AIS location and the nodal plane of the lowest-order harmonic function of the neuronal cell shape.

As seen in Figure 6, it is evident that the nodal plane of the lowest-order harmonic reasonably matches with the AnkG peak on the neurite showing a distal enriched Tau distribution in all these cases (Figure 6). Note that the calculation of the nodal plane location is solely based on cell shape, and yet it appears to discriminate between multiple AnkG-containing neurites in these rare situations.

AIS localization in a neuron with a collateral branch emerging from the nascent axon

Another interesting scenario arises when a single neuron is identified to possess a collateral branch emerging from the nascent axon in close proximity to the soma, as depicted in Figure 7. Notably, this collateral branch exhibits a comparable length to that of the nascent axon (the neurite with a distal enriched Tau distribution); however, the characteristic distal enrichment of Tau is absent within this collateral branch. This observation suggests two possibilities: either the collateral branch has yet to acquire axonal characteristics or it may develop into a dendrite in the future. Although a weaker AnkG cluster is observed near the initiation of the collateral branch, the nodal plane specifically colocalizes with the inner bound (closer to soma) of the major AnkG cluster along the neurite that developed a distal enriched Tau distribution.

DISCUSSION

Our results show that the location of the AnkG peak, which serves as a spatial marker of the AIS assembly site, is strongly correlated with the nodal plane of the lowest-order harmonic function of the neuronal cell shape—a purely geometric property—for the mouse hippocampal neurons *in vitro*. This suggests that an underlying mechanism exists to direct the AnkG proteins and establishment of the AIS to the nodal plane of the lowest-order harmonic produced by the neuron shape, potentially through regulation of the AnkG membrane partners or specific cytoskeletal structures. It further suggests that interactions with other neurons and extracellular factors may not be the sole determining factors for AIS assembly, given that our neurons are mostly isolated. Consequently, the influence of electrical activity, which is proposed to play a

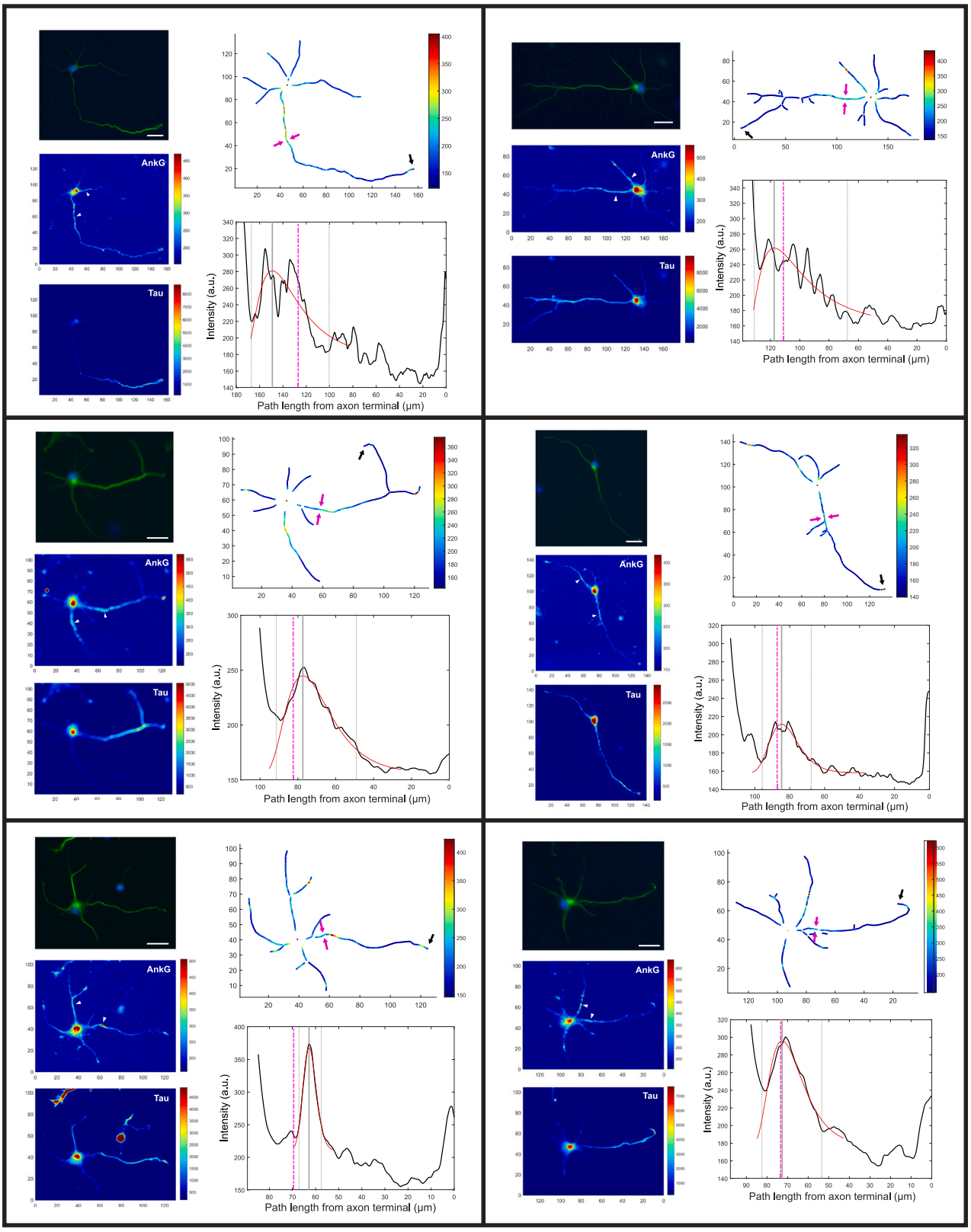
AnkG
Tau
Intensity (a.u.)
Path length from axon terminal (μm)

Figure 6. Nodal plane correlates with the neurite enriched in axon-specific Tau protein in neurons with two major AnkG clusters located on distinct neurites

In each panel, the first column shows the filtered β3-tubulin fluorescence image (green) merged with the DAPI fluorescence image (blue) (top), the AnkG fluorescence where the identified AnkG clusters are indicated by the white arrowheads (middle), and the Tau fluorescence for which the distal axonal distribution is evident (bottom). The first image in the second column of each panel shows the AnkG fluorescence intensity evaluated on the traced neuronal skeleton, with the nodal plane of the lowest-order harmonic marked by two opposite-facing magenta arrows, while the bottom image in the second column of each panel shows the smoothed AnkG intensity along the nascent axon, featuring elements similar to those shown in Figure 2. Scale bar: 20 μm.

role in AIS localization, might be relatively limited under our experimental conditions.[42,43] However, it is important to acknowledge that our experimental conditions do not completely eliminate all potential chemical interactions among the neurons. We note that the geometry of the neuron and the location of the AIS also influence neuronal excitability and the generation of the action potential as they control the electrical properties of the neuron.[44,45]

The majority of the developing mouse hippocampal neurons in our dataset are multipolar. Our analysis shows that there is a match between the AnkG peak position and the nodal plane of the lowest-order harmonic, with the nodal plane lying within the estimated AnkG-rich region for approximately 80% of the neurons. Given the highly heterogeneous population of hippocampal neurons,[46] this implies that the underlying geometry-sensing AIS localization mechanism is likely to be universal for all hippocampal neurons regardless of their functional types. The nodal plane tends to be located closer to soma than the corresponding AnkG peak, especially for neurons with shorter neurites. On average, the nodal planes have a ~4 μm shift from the AnkG peak toward the soma. This may suggest that the nodal plane is signaling an inner bound (closer to soma) for AnkG clustering rather than its center (i.e., the AnkG peak).

For neurons with longer neurites, the nodal plane tends to move away from the soma relative to the AnkG peak, and several possible explanations exist for this observation. One possibility is that the underlying geometry-sensing mechanism only triggers the onset of AnkG clustering, and, once the process is initiated and driven by a positive feedback loop, AnkG would then stabilize itself to its current position in coordination with its membrane and cytoskeletal partners. Its position thereby would no longer be tightly coupled to the neuron geometry. Alternatively, AIS could still be coupled to neuron shape but the coupling may not be tight; i.e., there could be other age-dependent factors that override fluctuations in the patterning system. Additionally, even if the nodal plane (AnkG assembly site) is shifted toward the axon terminal as the neuron matures, the relocation of the AnkG scaffold toward the distal axon may be hindered by the AnkB/α2/β2-spectrin scaffold backfilling from the axon terminal. Either possibility would reduce the strength of coupling between the AIS position and that of the nodal plane.

The correlation between the geometric property (nodal plane of the lowest-order harmonic function of the neuronal cell shape) and the location of the AIS (AnkG peak) is robustly maintained for exceptional neuron morphologies. Our analysis of the rare cases where neurons have multiple AnkG peaks on distinct neurites reveals that the nodal plane of the lowest-order harmonic correlates with the AnkG peak on the neurite showing a distal enriched Tau distribution, where the latter identifies the nascent axon. Thus, the nodal plane can distinguish the likely true axon and correctly place the AIS on this axon. Mislocalization of the AIS to dendrites can have catastrophic effects on proper neuronal function. Here we demonstrate that neurons can potentially discriminate between AnkG-containing neurites in these rare situations through a geometry-sensing mechanism, as this selection of the "correct" AIS assembly site is solely based on the shape of the neuron. Furthermore, the colocalization of the nodal plane of the lowest-order harmonic and the AnkG peak is observed in a neuron with a long collateral branch emerging near the soma from the nascent axon. Notably, the nodal plane exhibits a specific correlation with the inner bound of the major AnkG cluster on the neurite, which shows an enriched Tau distribution toward the distal end. While a minor AnkG peak, smaller in size and weaker in intensity, is present near the initiation of the collateral branch, the distal Tau enrichment is absent within this collateral branch. These findings provide additional evidence supporting the coupling between neuronal cell shape and AIS positioning and are also indicative that there is an interconnection between the establishment of the AIS and neuronal polarity.

Our analysis of the unique example of a neuron with an atypical morphology is particularly intriguing. The well-matched AnkG peak and nodal plane provide strong evidence that the AIS position is dictated by the shape of the neuron. This finding adds valuable insights to our understanding of AIS localization in different neuronal morphologies. However, we were only able to identify a single neuron of this type from the population, so additional data are needed to determine the generality of this observation. It is worth noting that the morphology and AIS location of this unique neuron resemble those of dorsal root ganglion (DRG) neurons, which represent one of the most extensively studied examples of pseudo-unipolar neurons due to their primary role in transmitting sensory signals.[47] Despite being less well characterized, cultured DRG neurons also contain an AIS-like region that is located within the stem axon and enriched in AnkG, βIV-spectrin, and various membrane partners such as NF-186 and Nav.[48–50] Conducting a similar analysis in established DRG neuron cultures would be a valuable advancement. However, such an investigation exceeds the scope of the current study.

Our ability to conduct a comprehensive analysis of the deviation between the nodal plane predictions and AIS measurements is limited by the accuracy of our data and its analysis. Although we have estimated the error of the nodal plane position by varying the soma compartment volume, we believe that the error may be underestimated, since there are other factors that could contribute to observed deviations. These factors include errors associated with AnkG peak detection, due to the diverse distributions of AnkG in early-developing neurons. Moreover, since neurons were traced from 2D images, small variations in the perpendicular direction of neurites may have been overlooked. Additionally, our model represents neurites as connected conical frustums, while in reality their shape and thickness may vary, especially near neurite terminals where growth cones are located. Lastly, for the calculation of lowest-order harmonics, we assumed that the diffusivities of molecules/proteins of interest are constant throughout the neuron. This assumption may oversimplify the real situation, as the intracellular environment in neurons is complex.

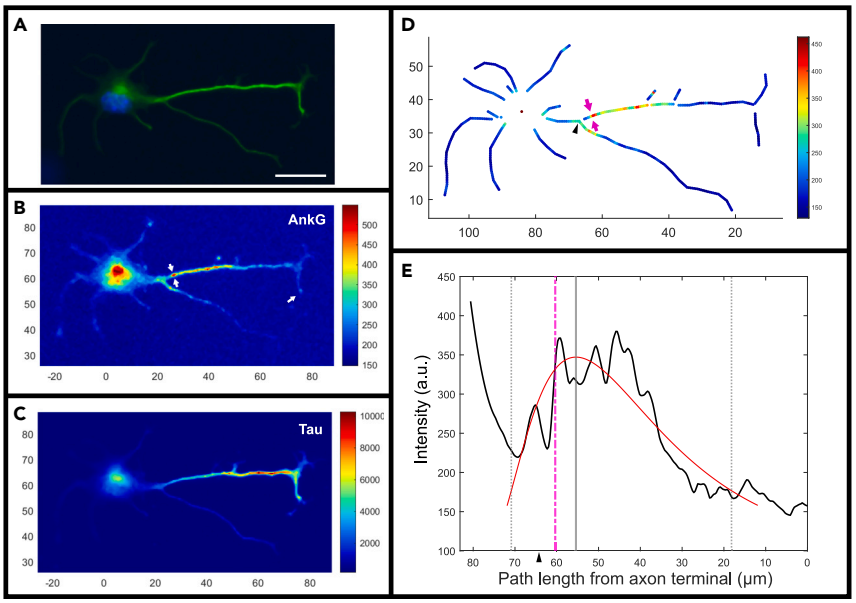

Figure 7. Colocalization of AIS and nodal plane in a neuron with a collateral branching from axonal shaft near soma

(A) The merged unfiltered fluorescence image of β3-tubulin fluorescence (green) and DAPI (blue).

(B) The AnkG fluorescence image.

(C) The Tau fluorescence image.

(D) The AnkG fluorescence intensity evaluated on the traced neuronal skeleton, with the nodal plane of the lowest-order harmonic marked by two opposite-facing magenta arrows.

(E) The plot of the smoothed AnkG intensity along the nascent axon, with features plotted in the same way as those shown in Figure 2. Note that the branchpoint, from which the collateral branch emerges, is indicated by the black arrowhead in panels (D) and (E). Scale bar: 20 μm.

Having established a correlation between the AIS location (and axon specification) and neuronal cell geometry, what geometry-sensing physical mechanisms could be responsible for such a correlation? Such a system would be an intracellular patterning system which establishes a spatial or spatiotemporal molecular pattern controlled by the shape of the bounding cell membrane and/or cellular structures (e.g., cytoskeleton). Experimental observations have demonstrated that the mechanism establishing neuronal polarity is dynamic *in vitro*.[6,8–10] Although the corresponding dynamics of the AIS in these experiments remains elusive, our observations on neurons containing multiple AnkG peaks, combined with the fact that AIS regenerates *in vivo*,[12,13] lead us to believe that the assembly of the AIS is coupled to the establishment of neuronal polarity in a yet-to-be-determined manner.

Several mathematical models have been proposed to explain the establishment of neuronal polarity. One class of models involves the active transport of various molecules in addition to a reaction-diffusion system.[51–53] While these models can respond dynamically to changes in neuron shape, they cannot explain the formation of the AIS, at least not in a clear way. One possible approach to account for AIS positioning in these models is to introduce components that sense chemical concentration gradients down the axon. However, this would require fine-tuning of the concentration threshold for the AIS assembly as the axon grows; thus the robustness of such a mechanism is subject to questioning.

On the other hand, reaction-diffusion systems with a local activation-global inhibition mechanism or Turing patterning mechanisms have also been proposed for establishment of neuronal polarity,[54–56] albeit only at a conceptual level or through studies using simplified toy neuron models. While active transport dominates over long distances and timescales that are important for mature neurons, it is not necessarily required for pattern formation in immature/developing neurons. In addition, the existence of active transport-based mechanisms does not rule out the possibility of a Turing mechanism operating in parallel with or preceding it during early neuronal development. Regardless of the complexity of specific Turing patterning systems, they share common features in being coupled to the cell shape and size. According to linear instability analysis, the Turing pattern generally arises as a linear combination of the first few lowest-order harmonic modes, which are determined by the cell shape.[34,35]

To date, the bacterial Min proteins constitute the best-characterized model system for studying intracellular Turing patterning mechanisms that establish the location of a major cellular structure: the cell division ring in the case of the Min system.[32,57,58] In this system, the Min proteins dynamically create a spatiotemporal concentration pattern that oscillates from pole to pole in rod-shaped cells[59] inhibiting cell division (FtsZ-ring formation) at the poles, thus localizing the cell division plane to the center of the cell.[60,61] The Min patterning system can be regenerated *in vitro* using only two proteins: a membrane-binding ATPase, MinD, and its activator, MinE, where the ATPase reaction controls whether MinD is cytosolic or membrane bound.[62] The pattern formed by the Min system is dynamically dictated by the geometry and size of the cell,[63] in which the division plane placement can be predicted by the nodal plane of the lowest-order harmonic function of the cell

shape.[34] Recently, an intracellular patterning system that senses cell size and shape has been implicated in regulating cell division plane placement in pleomorphic archaeal cells.[33] Other protein systems have been shown to generate oscillating spatial patterns in archaea.[64] Thus, it is evident from these examples that Turing patterning mechanisms can provide a direct link between the nodal plane of the lowest-order harmonic and the localization of intracellular structures like the cell division ring.

Although neurons do not divide, we speculate that a similar intracellular patterning system could be in place to regulate AIS assembly. In neurons, one candidate system that is potentially Turing-like and involved in the establishment of neuronal polarity or AIS localization is the Par3/Par6/aPKC system,[65] which has also been shown to play a role in establishing apical-basal polarity of epithelial cells.[66]

Can a Turing mechanism account for the establishment of axonal polarity and AIS localization in developing neurons? Neurons differ from archaea and bacteria in that they do not undergo cell division and renewal and can grow to lengths ranging from a millimeter to over a meter, depending on the type of neuron, which is many times larger than their immature forms. Since the modes of a putative Turing pattern are coupled to the neuron's dimension, it begs the question of why higher-order Turing modes in mature neurons do not cause the formation of multiple AISs. One solution to this dilemma is that, once neuronal polarity is established, this polarization prevents the formation of additional AIS-like structures. While the nodal planes of higher-order harmonics modes can occur on different neurites, it is unlikely that the formation of a new AIS can occur on dendrites due to a lack of the necessary submembranous actin/spectrin scaffold in the dendritic compartment after polarity has been established. On the other hand, if such putative higher-order nodal planes were to be located on the axon, the formation of a new AIS would be blocked due to the occupancy of AnkB along the axon. AnkG and AnkB are mutually exclusive, meaning that AnkB would prevent AnkG from being localized to the same area. Thus, once the cortical actin-spectrin structure is formed, it likely locks in both the axonal compartment and the AIS location.

Another possibility is that the putative underlying Turing system is dynamically regulated and is only responsible for the onset of AIS formation. Once the AIS and molecular sorting mechanisms are properly established in the mature neuron, the Turing system may be turned off through age-dependent regulation or a feedback mechanism. This is also consistent with the fact that mature neurons tend to lose their ability to regenerate a new axon after axotomy. However, these are just speculations at this stage.

Currently, our understanding of the AIS assembly is limited, and there is still much to learn about the underlying mechanisms. The proteins involved in these processes remain unclear, but the nature of the Turing mechanism could help to narrow down the scope of potential candidates. For a Turing pattern to form, energy input is required to drive the system away from equilibrium, and there has to be a significant difference in diffusivities. The former usually means one of the proteins in the system should be an ATPase or a GTPase, where the nature of the bound nucleotide (nucleoside triphosphate (NTP) versus nucleoside diphosphate (NDP)) controls binding to the membrane or the cytoskeletal scaffold, thus coupling changes in diffusion coefficient to the bound nucleotide state (NTP or NDP) which is controlled via the enzymatic activity. We note that the Par3/Par6/APC system meets these required properties.

Based on our current results, we speculate that a dynamic intracellular patterning system such as a Turing or reaction-diffusion system could provide the universal mechanism involved in directing AIS assembly to the proximal axon, regardless of neuron type. However, a larger dataset is required to support this argument. To further confirm these results, future studies using 3D time-lapse fluorescence microscopy will help to increase the accuracy of our analysis and characterize the dynamical response of the AIS as the neuron matures or as neuronal morphology changes.

Limitations of the study

One limitation in extending the high-throughput AIS localization analysis to organized tissue, such as organotypic slices and *in vivo* studies, is the requirement for intact, isolated neuronal morphology. While achieving this is feasible with state-of-the-art tissue clearing techniques, as reviewed by Ueda et al.,[67] it demands significant additional effort. It is crucial to note that the current study exclusively focuses on mouse hippocampal neurons. Further investigation is needed to determine whether the same correspondence between AIS localizations and nodal planes exists across all neuron types and animal models. Moreover, although we propose the Turing patterning system as a potential mechanism dynamically governing the localization of AIS assembly, it may not be the only mechanism that can reproduce the observed correspondence. Lastly, with the current experimental setup, albeit excluding neurons with direct physical contact with other cells, there remains a possibility of extracellular stimuli affecting AIS assembly for the analyzed neurons. This could occur through the transmission of signals via growth medium. Therefore, to validate the findings of the present study, future research should employ more advanced techniques aimed at fully isolating individual neurons.

STAR★METHODS

Detailed methods are provided in the online version of this paper and include the following:

- KEY RESOURCES TABLE
- RESOURCE AVAILABILITY
  - Lead contact
  - Materials availability
  - Data and code availability
- EXPERIMENTAL MODEL AND STUDY PARTICIPANT DETAILS
  - Animals

- METHOD DETAILS
  - Culture of hippocampal neurons
  - Immunocytochemistry
  - High-throughput neuron shape detection
  - Semi-automated neuronal tracing
  - Neuron model and computation of the lowest order harmonic
  - Analysis of AnkG cluster
  - Derivation of the discrete laplacian
  - Numerical validation of the discrete laplacian approach
  - Impact of soma shape on nodal plane position
- QUANTIFICATION AND STATISTICAL ANALYSIS

SUPPLEMENTAL INFORMATION

Supplemental information can be found online at https://doi.org/10.1016/j.isci.2024.109264.

ACKNOWLEDGMENTS

This research was funded by the Australian Research Council grants (DP180101473 to T.F. and DP 200100345 to C.N.A.) and the Australian National Health and Medical Research Council (APP200660 to T.F.). Z.X. was supported by a scholarship from the Australian Government Research Training Program.

AUTHOR CONTRIBUTIONS

Z.X., C.N.A., and P.M.G.C. conceived and designed the study. H.S., E.P., and T.F. performed the experiment and acquired neuron data. Z.X., C.N.A., and Y.W. designed the mathematical model and the computational framework. Z.X. and Y.W. processed and analyzed the data. Z.X. drafted the manuscript. P.M.G.C. and C.N.A. supervised the project. All authors have reviewed and approved the final manuscript.

DECLARATION OF INTERESTS

The authors declare no competing interests.

Received: September 28, 2023
Revised: December 21, 2023
Accepted: February 14, 2024
Published: February 17, 2024

REFERENCES

1. Leterrier, C. (2018). The Axon Initial Segment: An Updated Viewpoint. J. Neurosci. *38*, 2135–2145. https://doi.org/10.1523/jneurosci.1922-17.2018.
2. Wiggin, G.R., Fawcett, J.P., and Pawson, T. (2005). Polarity proteins in axon specification and synaptogenesis. Dev. Cell *8*, 803–816. https://doi.org/10.1016/j.devcel.2005.05.007.
3. Stanganello, E., Zahavi, E.E., Burute, M., Smits, J., Jordens, I., Maurice, M.M., Kapitein, L.C., and Hoogenraad, C.C. (2019). Wnt Signaling Directs Neuronal Polarity and Axonal Growth. iScience *13*, 318–327. https://doi.org/10.1016/j.isci.2019.02.029.
4. Bolós, M., Terreros-Roncal, J., Perea, J.R., Pallas-Bazarra, N., Ávila, J., and Llorens-Martín, M. (2019). Maturation Dynamics of the Axon Initial Segment (AIS) of Newborn Dentate Granule Cells in Young Adult C57BL/6J Mice. J. Neurosci. *39*, 1605–1620. https://doi.org/10.1523/JNEUROSCI.2253-18.2019.
5. Dotti, C.G., Sullivan, C.A., and Banker, G.A. (1988). The establishment of polarity by hippocampal neurons in culture. J. Neurosci. *8*, 1454–1468.
6. Goslin, K., and Banker, G. (1989). Experimental observations on the development of polarity by hippocampal neurons in culture. J. Cell Biol. *108*, 1507–1516. https://doi.org/10.1083/jcb.108.4.1507.
7. Zhong, G., He, J., Zhou, R., Lorenzo, D., Babcock, H.P., Bennett, V., and Zhuang, X. (2014). Developmental mechanism of the periodic membrane skeleton in axons. Elife *3*, e04581. https://doi.org/10.7554/eLife.04581.
8. Dotti, C.G., and Banker, G.A. (1987). Experimentally induced alteration in the polarity of developing neurons. Nature *330*, 254–256. https://doi.org/10.1038/330254a0.
9. Bradke, F., and Dotti, C.G. (2000). Differentiated neurons retain the capacity to generate axons from dendrites. Curr. Biol. *10*, 1467–1470. https://doi.org/10.1016/s0960-9822(00)00807-1.
10. Bradke, F., and Dotti, C.G. (1997). Neuronal polarity: vectorial cytoplasmic flow precedes axon formation. Neuron *19*, 1175–1186. https://doi.org/10.1016/s0896-6273(00)80410-9.
11. Gomis-Rüth, S., Wierenga, C.J., and Bradke, F. (2008). Plasticity of polarization: changing dendrites into axons in neurons integrated in neuronal circuits. Curr. Biol. *18*, 992–1000. https://doi.org/10.1016/j.cub.2008.06.026.
12. Kiryu-Seo, S., Matsushita, R., Tashiro, Y., Yoshimura, T., Iguchi, Y., Katsuno, M., Takahashi, R., and Kiyama, H. (2022). Impaired disassembly of the axon initial segment restricts mitochondrial entry into damaged axons. EMBO J. *41*, e110486. https://doi.org/10.15252/embj.2021110486.
13. Marin, M.A., de Lima, S., Gilbert, H.Y., Giger, R.J., Benowitz, L., and Rasband, M.N. (2016). Reassembly of Excitable Domains after CNS Axon Regeneration. J. Neurosci. *36*, 9148–9160. https://doi.org/10.1523/jneurosci.1747-16.2016.
14. Evans, M.D., Tufo, C., Dumitrescu, A.S., and Grubb, M.S. (2017). Myosin II activity is required for structural plasticity at the axon initial segment. Eur. J. Neurosci. *46*, 1751–1757. https://doi.org/10.1111/ejn.13597.
15. Abouelezz, A., Stefen, H., Segerstråle, M., Micinski, D., Minkeviciene, R., Lahti, L., Hardeman, E.C., Gunning, P.W., Hoogenraad, C.C., Taira, T., et al. (2020). Tropomyosin Tpm3.1 Is Required to Maintain the Structure and Function of the Axon Initial Segment. iScience *23*, 101053. https://doi.org/10.1016/j.isci.2020.101053.
16. Zhang, W., Ciorraga, M., Mendez, P., Retana, D., Boumedine-Guignon, N., Achón, B., Russier, M., Debanne, D., and Garrido, J.J. (2021). Formin Activity and mDia1 Contribute to Maintain Axon Initial Segment Composition and Structure. Mol. Neurobiol.

58, 6153–6169. https://doi.org/10.1007/s12035-021-02531-6.

17. Galiano, M.R., Jha, S., Ho, T.S.Y., Zhang, C., Ogawa, Y., Chang, K.J., Stankewich, M.C., Mohler, P.J., and Rasband, M.N. (2012). A distal axonal cytoskeleton forms an intra-axonal boundary that controls axon initial segment assembly. Cell *149*, 1125–1139. https://doi.org/10.1016/j.cell.2012.03.039.
18. Xu, X., and Shrager, P. (2005). Dependence of axon initial segment formation on Na+ channel expression. J. Neurosci. Res. *79*, 428–441. https://doi.org/10.1002/jnr.20378.
19. Zonta, B., Desmazieres, A., Rinaldi, A., Tait, S., Sherman, D.L., Nolan, M.F., and Brophy, P.J. (2011). A critical role for Neurofascin in regulating action potential initiation through maintenance of the axon initial segment. Neuron *69*, 945–956. https://doi.org/10.1016/j.neuron.2011.02.021.
20. Leterrier, C., Clerc, N., Rueda-Boroni, F., Montersino, A., Dargent, B., and Castets, F. (2017). Ankyrin G Membrane Partners Drive the Establishment and Maintenance of the Axon Initial Segment. Front. Cell. Neurosci. *11*, 6. https://doi.org/10.3389/fncel.2017.00006.
21. Lasiecka, Z.M., Yap, C.C., Vakulenko, M., and Winckler, B. (2009). Compartmentalizing the neuronal plasma membrane from axon initial segments to synapses. Int. Rev. Cell Mol. Biol. *272*, 303–389. https://doi.org/10.1016/S1937-6448(08)01607-9.
22. Kapitein, L.C., and Hoogenraad, C.C. (2011). Which way to go? Cytoskeletal organization and polarized transport in neurons. Mol. Cell. Neurosci. *46*, 9–20. https://doi.org/10.1016/j.mcn.2010.08.015.
23. Kosik, K.S., Orecchio, L.D., Bakalis, S., and Neve, R.L. (1989). Developmentally regulated expression of specific tau sequences. Neuron *2*, 1389–1397. https://doi.org/10.1016/0896-6273(89)90077-9.
24. Bentley, M., and Banker, G. (2016). The cellular mechanisms that maintain neuronal polarity. Nat. Rev. Neurosci. *17*, 611–622. https://doi.org/10.1038/nrn.2016.100.
25. Fache, M.P., Moussif, A., Fernandes, F., Giraud, P., Garrido, J.J., and Dargent, B. (2004). Endocytotic elimination and domain-selective tethering constitute a potential mechanism of protein segregation at the axonal initial segment. J. Cell Biol. *166*, 571–578. https://doi.org/10.1083/jcb.200312155.
26. Brachet, A., Leterrier, C., Irondelle, M., Fache, M.P., Racine, V., Sibarita, J.B., Choquet, D., and Dargent, B. (2010). Ankyrin G restricts ion channel diffusion at the axonal initial segment before the establishment of the diffusion barrier. J. Cell Biol. *191*, 383–395. https://doi.org/10.1083/jcb.201003042.
27. Benned-Jensen, T., Christensen, R.K., Denti, F., Perrier, J.F., Rasmussen, H.B., and Olesen, S.P. (2016). Live Imaging of Kv7.2/7.3 Cell Surface Dynamics at the Axon Initial Segment: High Steady-State Stability and Calpain-Dependent Excitotoxic Downregulation Revealed. J. Neurosci. *36*, 2261–2266. https://doi.org/10.1523/JNEUROSCI.2631-15.2016.
28. Torii, T., Ogawa, Y., Liu, C.H., Ho, T.S.Y., Hamdan, H., Wang, C.C., Oses-Prieto, J.A., Burlingame, A.L., and Rasband, M.N. (2020). NuMA1 promotes axon initial segment assembly through inhibition of endocytosis. J. Cell Biol. *219*, e201907048. https://doi.org/10.1083/jcb.201907048.
29. Fréal, A., Rai, D., Tas, R.P., Pan, X., Katrukha, E.A., van de Willige, D., Stucchi, R., Aher, A., Yang, C., Altelaar, A.F.M., et al. (2019). Feedback-Driven Assembly of the Axon Initial Segment. Neuron *104*, 305–321.e8. https://doi.org/10.1016/j.neuron.2019.07.029.
30. Moseley, J.B., and Nurse, P. (2010). Cell division intersects with cell geometry. Cell *142*, 184–188. https://doi.org/10.1016/j.cell.2010.07.004.
31. Bähler, J., and Pringle, J.R. (1998). Pom1p, a fission yeast protein kinase that provides positional information for both polarized growth and cytokinesis. Genes Dev. *12*, 1356–1370. https://doi.org/10.1101/gad.12.9.1356.
32. Bonny, M., Fischer-Friedrich, E., Loose, M., Schwille, P., and Kruse, K. (2013). Membrane binding of MinE allows for a comprehensive description of Min-protein pattern formation. PLoS Comput. Biol. *9*, e1003347. https://doi.org/10.1371/journal.pcbi.1003347.
33. Walsh, J.C., Angstmann, C.N., Bisson-Filho, A.W., Garner, E.C., Duggin, I.G., and Curmi, P.M.G. (2019). Division plane placement in pleomorphic archaea is dynamically coupled to cell shape. Mol. Microbiol. *112*, 785–799. https://doi.org/10.1111/mmi.14316.
34. Walsh, J.C., Angstmann, C.N., Duggin, I.G., and Curmi, P.M.G. (2017). Non-linear Min protein interactions generate harmonics that signal mid-cell division in Escherichia coli. PLoS One *12*, e0185947. https://doi.org/10.1371/journal.pone.0185947.
35. Turing, A.M. (1990). The chemical basis of morphogenesis. 1953. Bull. Math. Biol. *52*, 153. , discussion 119-152. https://doi.org/10.1007/BF02459572.
36. Boss, D., Hoffmann, A., Rappaz, B., Depeursinge, C., Magistretti, P.J., Van de Ville, D., and Marquet, P. (2012). Spatially-resolved eigenmode decomposition of red blood cells membrane fluctuations questions the role of ATP in flickering. PLoS One *7*, e40667. https://doi.org/10.1371/journal.pone.0040667.
37. Fath, T., Ke, Y.D., Gunning, P., Götz, J., and Ittner, L.M. (2009). Primary support cultures of hippocampal and substantia nigra neurons. Nat. Protoc. *4*, 78–85. https://doi.org/10.1038/nprot.2008.199.
38. Kole, M.H.P., and Stuart, G.J. (2012). Signal processing in the axon initial segment. Neuron *73*, 235–247. https://doi.org/10.1016/j.neuron.2012.01.007.
39. Yang, R., Walder-Christensen, K.K., Lalani, S., Yan, H., García-Prieto, I.D., Álvarez, S., Fernández-Jaén, A., Speltz, L., Jiang, Y.H., and Bennett, V. (2019). Neurodevelopmental mutation of giant ankyrin-G disrupts a core mechanism for axon initial segment assembly. Proc. Natl. Acad. Sci. USA *116*, 19717–19726. https://doi.org/10.1073/pnas.1909989116.
40. Jiang, H., Guo, W., Liang, X., and Rao, Y. (2005). Both the establishment and the maintenance of neuronal polarity require active mechanisms: critical roles of GSK-3beta and its upstream regulators. Cell *120*, 123–135. https://doi.org/10.1016/j.cell.2004.12.033.
41. Guo, Y., Liu, Z., Chen, Y.-K., Chai, Z., Zhou, C., and Zhang, Y. (2017). Neurons with Multiple Axons Have Functional Axon Initial Segments. Neurosci. Bull. *33*, 641–652. https://doi.org/10.1007/s12264-017-0169-3.
42. Grubb, M.S., and Burrone, J. (2010). Activity-dependent relocation of the axon initial segment fine-tunes neuronal excitability. Nature *465*, 1070–1074. https://doi.org/10.1038/nature09160.
43. Gulledge, A.T., and Bravo, J.J. (2016). Neuron Morphology Influences Axon Initial Segment Plasticity. eneuro *3*. ENEURO.0085, 15.2016. https://doi.org/10.1523/eneuro.0085-15.2016.
44. Goethals, S., Sierksma, M.C., Nicol, X., Réaux-Le Goazigo, A., and Brette, R. (2021). Electrical match between initial segment and somatodendritic compartment for action potential backpropagation in retinal ganglion cells. J. Neurophysiol. *126*, 28–46. https://doi.org/10.1152/jn.00005.2021.
45. Fékété, A., Ankri, N., Brette, R., and Debanne, D. (2021). Neural excitability increases with axonal resistance between soma and axon initial segment. Proc. Natl. Acad. Sci. USA *118*, e2102217118. https://doi.org/10.1073/pnas.2102217118.
46. Wheeler, D.W., White, C.M., Rees, C.L., Komendantov, A.O., Hamilton, D.J., and Ascoli, G.A. (2015). Hippocampome.org: a knowledge base of neuron types in the rodent hippocampus. Elife *4*, e09960. https://doi.org/10.7554/eLife.09960.
47. Nascimento, A.I., Mar, F.M., and Sousa, M.M. (2018). The intriguing nature of dorsal root ganglion neurons: Linking structure with polarity and function. Prog. Neurobiol. *168*, 86–103. https://doi.org/10.1016/j.pneurobio.2018.05.002.
48. Zhang, X., and Bennett, V. (1998). Restriction of 480/270-kD ankyrin G to axon proximal segments requires multiple ankyrin G-specific domains. J. Cell Biol. *142*, 1571–1581. https://doi.org/10.1083/jcb.142.6.1571.
49. Hedstrom, K.L., Xu, X., Ogawa, Y., Frischknecht, R., Seidenbecher, C.I., Shrager, P., and Rasband, M.N. (2007). Neurofascin assembles a specialized extracellular matrix at the axon initial segment. J. Cell Biol. *178*, 875–886. https://doi.org/10.1083/jcb.200705119.
50. Dzhashiashvili, Y., Zhang, Y., Galinska, J., Lam, I., Grumet, M., and Salzer, J.L. (2007). Nodes of Ranvier and axon initial segments are ankyrin G-dependent domains that assemble by distinct mechanisms. J. Cell Biol. *177*, 857–870. https://doi.org/10.1083/jcb.200612012.
51. Graham, B.P., and van Ooyen, A. (2006). Mathematical modelling and numerical simulation of the morphological development of neurons. BMC Neurosci. *7*, S9. https://doi.org/10.1186/1471-2202-7-S1-S9.
52. Toriyama, M., Sakumura, Y., Shimada, T., Ishii, S., and Inagaki, N. (2010). A diffusion-based neurite length-sensing mechanism involved in neuronal symmetry breaking. Mol. Syst. Biol. *6*, 394. https://doi.org/10.1038/msb.2010.51.
53. Naoki, H., Nakamuta, S., Kaibuchi, K., and Ishii, S. (2011). Flexible search for single-axon morphology during neuronal spontaneous polarization. PLoS One *6*, e19034. https://doi.org/10.1371/journal.pone.0019034.
54. Andersen, S.S., and Bi, G.Q. (2000). Axon formation: a molecular model for the generation of neuronal polarity. Bioessays *22*, 172–179. https://doi.org/10.1002/(SICI)1521-1878(200002)22:2<172::AID-BIES8>3.0.CO;2-Q.
55. Menchón, S.A., Gärtner, A., Román, P., and Dotti, C.G. (2011). Neuronal (bi)polarity as a self-organized process enhanced by growing membrane. PLoS One *6*, e24190. https://doi.org/10.1371/journal.pone.0024190.

56. Chen, C., Wirth, A., and Ponimaskin, E. (2012). Cdc42: an important regulator of neuronal morphology. Int. J. Biochem. Cell Biol. *44*, 447–451. https://doi.org/10.1016/j.biocel.2011.11.022.
57. Kruse, K., Howard, M., and Margolin, W. (2007). An experimentalist's guide to computational modelling of the Min system. Mol. Microbiol. *63*, 1279–1284. https://doi.org/10.1111/j.1365-2958.2007.05607.x.
58. Walsh, J.C., Angstmann, C.N., Duggin, I.G., and Curmi, P.M.G. (2015). Molecular Interactions of the Min Protein System Reproduce Spatiotemporal Patterning in Growing and Dividing Escherichia coli Cells. PLoS One *10*, e0128148. https://doi.org/10.1371/journal.pone.0128148.
59. Yu, X.C., and Margolin, W. (1999). FtsZ ring clusters in min and partition mutants: role of both the Min system and the nucleoid in regulating FtsZ ring localization. Mol. Microbiol. *32*, 315–326. https://doi.org/10.1046/j.1365-2958.1999.01351.x.
60. Bi, E., and Lutkenhaus, J. (1993). Cell division inhibitors SulA and MinCD prevent formation of the FtsZ ring. J. Bacteriol. *175*, 1118–1125. https://doi.org/10.1128/jb.175.4.1118-1125.1993.
61. Ramm, B., Heermann, T., and Schwille, P. (2019). The E. coli MinCDE system in the regulation of protein patterns and gradients. Cell. Mol. Life Sci. *76*, 4245–4273. https://doi.org/10.1007/s00018-019-03218-x.
62. Loose, M., Fischer-Friedrich, E., Ries, J., Kruse, K., and Schwille, P. (2008). Spatial regulators for bacterial cell division self-organize into surface waves in vitro. Science *320*, 789–792. https://doi.org/10.1126/science.1154413.
63. Wu, F., van Schie, B.G.C., Keymer, J.E., and Dekker, C. (2015). Symmetry and scale orient Min protein patterns in shaped bacterial sculptures. Nat. Nanotechnol. *10*, 719–726. https://doi.org/10.1038/nnano.2015.126.
64. Nußbaum, P., Ithurbide, S., Walsh, J.C., Patro, M., Delpech, F., Rodriguez-Franco, M., Curmi, P.M.G., Duggin, I.G., Quax, T.E.F., and Albers, S.V. (2020). An Oscillating MinD Protein Determines the Cellular Positioning of the Motility Machinery in Archaea. Curr. Biol. *30*, 4956–4972.e4. https://doi.org/10.1016/j.cub.2020.09.073.
65. Funahashi, Y., Watanabe, T., and Kaibuchi, K. (2020). Advances in defining signaling networks for the establishment of neuronal polarity. Curr. Opin. Cell Biol. *63*, 76–87. https://doi.org/10.1016/j.ceb.2019.12.009.
66. Joberty, G., Petersen, C., Gao, L., and Macara, I.G. (2000). The cell-polarity protein Par6 links Par3 and atypical protein kinase C to Cdc42. Nat. Cell Biol. *2*, 531–539. https://doi.org/10.1038/35019573.
67. Ueda, H.R., Ertürk, A., Chung, K., Gradinaru, V., Chédotal, A., Tomancak, P., and Keller, P.J. (2020). Tissue clearing and its applications in neuroscience. Nat. Rev. Neurosci. *21*, 61–79. https://doi.org/10.1038/s41583-019-0250-1.
68. Peng, H., Ruan, Z., Long, F., Simpson, J.H., and Myers, E.W. (2010). V3D enables real-time 3D visualization and quantitative analysis of large-scale biological image data sets. Nat. Biotechnol. *28*, 348–353. https://doi.org/10.1038/nbt.1612.
69. Xiao, H., and Peng, H. (2013). APP2: automatic tracing of 3D neuron morphology based on hierarchical pruning of a gray-weighted image distance-tree. Bioinformatics *29*, 1448–1454. https://doi.org/10.1093/bioinformatics/btt170.
70. Lorensen, W.E., and Cline, H.E. (1987). Marching Cubes: A High Resolution 3D Surface Construction Algorithm. ACM SIGGRAPH Computer Graphics *21*, 163. https://doi.org/10.1145/37401.37422.
71. Reuter, M., Wolter, F.-E., and Peinecke, N. (2006). Laplace–Beltrami spectra as 'Shape-DNA' of surfaces and solids. Comput. Aided Des. *38*, 342–366.
72. Garland, M., and Heckbert, P.S. (1997). Surface Simplification Using Quadric Error Metrics. Proceedings of the 24th Annual Conference on Computer Graphics and Interactive Techniques (ACM Press/Addison-Wesley Publishing Co).
73. Geuzaine, C., and Remacle, J.-F. (2009). Gmsh: A 3-D finite element mesh generator with built-in pre- and post-processing facilities. Int. J. Numer. Methods Eng. *79*, 1309–1331.
74. Cooper, G.M. (2000). The Cell: A Molecular Approach, 2nd ed. Edition (ASM Press Sunderland, Mass: Sinauer Associates).
75. Wang, R., and Brattain, M.G. (2007). The maximal size of protein to diffuse through the nuclear pore is larger than 60kDa. FEBS Lett. *581*, 3164–3170. https://doi.org/10.1016/j.febslet.2007.05.082.

STAR★METHODS

KEY RESOURCES TABLE

REAGENT or RESOURCE	SOURCE	IDENTIFIER
Antibodies		
Ankyrin-G	Merck	Cat#MABN466; RRID: AB2749806
Tau	rPeptide	Cat#TA-3020-1
Beta III Tubulin	Abcam	Cat#ab41489; RRID: AB_727049
Donkey anti-Mouse IgG (H + L) Highly Cross-Adsorbed Secondary Antibody, Alexa Fluor™ 488	ThermoFisher	Cat#A-21202; RRID: AB_141607
Donkey anti-Rabbit IgG (H + L) Highly Cross-Adsorbed Secondary Antibody, Alexa Fluor™ 555	ThermoFisher	Cat#A-31572; RRID: AB_162543
Goat anti-Chicken IgY (H + L) Secondary Antibody, Alexa Fluor™ 647	ThermoFisher	Cat#A-21449; RRID: AB_2535866
Chemicals, peptides, and recombinant proteins		
Poly-D-lysine hydrobromide	Sigma-Aldrich	Cat#P0899
Hanks balanced salt solution	Sigma-Aldrich	Cat#H4641
Deoxyribonuclease I from bovine pancreas	Sigma-Aldrich	Cat#DN25
Trypsin solution from porcine pancreas	Sigma-Aldrich	Cat#T4549
DMEM, high glucose, no glutamine	ThermoFisher	Cat#11960069
Fetal Bovine Serum, certified, United States	ThermoFisher	Cat#16000044
Neurobasal™ Medium	ThermoFisher	Cat#21103049
B-27™ Supplement (50X), serum free	ThermoFisher	Cat#17504044
GlutaMAX™ Supplement	ThermoFisher	Cat#35050061
DAPI	ThermoFisher	Cat#D1306
Experimental models: Organisms/strains		
C57Bl/6J mice	Animal Resource Center (ARC)	ARC has now been acquired by Ozgene ARC
Software and algorithms		
MATLAB Version 2019b	MathWorks	https://www.mathworks.com/
Vaa3D	Howard Hughes Medical Institute (Peng et al.[68])	http://home.penglab.com/proj/vaa3d/home/index.html
Other		
NeuronHarmonicAnalysis	This paper	https://github.com/ZhuangGitRepo/Neuron_AIS_Analysis

RESOURCE AVAILABILITY

Lead contact

Further information and requests for resources related to this study should be directed to, and will be fulfilled by, the lead contact Paul Curmi (p.curmi@unsw.edu.au).

Materials availability

This study did not generate new unique reagents.

Data and code availability

- All data reported in this paper will be shared by the lead contact upon reasonable request.
- All original code has been deposited at https://github.com/ZhuangGitRepo/Neuron_AIS_Analysis.
- Any additional information required to reanalyze the data reported in this paper is available from the lead contact upon request.

EXPERIMENTAL MODEL AND STUDY PARTICIPANT DETAILS

Animals

Procedures involving animals were conducted in accordance with national and international guidelines and approved by Macquarie University Animal Care and Ethics Committee. Time-mated C57BL/6J mice were acquired from the Animal Resource Center (Perth, Australia). Upon delivery, pregnant dams were housed in ventilated cages with *ad libitum* access to food and water and maintained on a 12-h light cycle. Euthanasia by cervical dislocation was carried out at gestational day 16.

METHOD DETAILS

Culture of hippocampal neurons

Low-density mouse hippocampal neurons were prepared as per the protocol.[37] In short, the hippocampi were dissected from the brains of mixed gender embryonic mice at embryonic day 16 (E16) and dissociated by mechanical trituration after enzymatic exposure to trypsin and DNase I (Sigma-Aldrich). Hippocampal neurons were plated and immobilized at a density of 5,000 cells/coverslip on PDL-coated 13 mm glass coverslips in 12 well plastic plates (Corning) in Dulbecco's Modified Eagle Medium (DMEM, ThermoFisher) with 10% fetal bovine serum (FBS, ThermoFisher). A cortical support ring of 150,000 cells/100 μL was plated in a ring around the perimeter of the well to provide trophic support for the growth of the hippocampal neurons. Cultures were maintained in neurobasal media supplemented with 2% B27 supplements and 2 mM Glutamax (ThermoFisher) at 37°C and 5% CO_2.

Immunocytochemistry

Hippocampal cultures were fixed at 3, 5, 7 and 10 days *in vitro* (DIV) with 4% paraformaldehyde (PFA) for 15 min at room temperature before permeabilization with 0.1% Triton X-100 in PBS for 5 min. Cells were then blocked in 2% FBS in PBS. Incubation with primary antibodies was overnight at 4°C: mouse anti-ankyrin G (1:500, Abcam), rabbit anti-Tau (1:40,000, rPeptide), chicken anti-β3 tubulin (1:300, Merck). Prior to addition of the secondary antibodies, coverslips were washed 5 times with PBS. Coverslips were then incubated with secondary antibodies for 1 h at room temperature. All secondary antibodies were diluted to a concentration of 1:500 (ThermoFisher): donkey anti-mouse Alexa 488, donkey anti-rabbit Alexa 555, and goat anti-chicken Alexa 647. Primary and secondary antibodies were diluted in the blocking solution. After secondary antibody incubation, coverslips were washed 5 times with PBS and DAPI (1:1000) was added for 30 min at RT. Coverslips were then mounted on glass slides using DAKO mounting media and imaged using a 20× air objective on an Axio Scan Z1 slide scanner microscope (Zeiss) and a 60× oil objective on a BX51 microscope (Olympus).

High-throughput neuron shape detection

The microscope images of the mouse hippocampal neurons were analyzed using MATLAB. The original multi-channel images of the neuron coverslips (38,249 × 38,813 pixels) were first split into 5 × 5 tiles. The β3-tubulin channel of each tiled image was then preprocessed using a top-hat transform with a disk-shaped structuring element with a radius of 30 pixels for the kernel. Individual neurons were identified through a thresholding-based binarization of β3-tubulin images, followed by the application of the 'bwconncomp' function in MATLAB. Subsequently, the binarized neuron shapes underwent dilation using a disk-shaped structuring element with a radius of 7 pixels (pixel size = 325nm). The resulting filtered β3-tubulin images for neuronal tracing were generated by extracting the regions corresponding to the dilated neuron shapes from the original β3-tubulin images.

Meanwhile, the DAPI channel was also thresholded by the average background DAPI intensity. There were generally two ways that the neurons could be in physical contact with each other: the neurites of two separate neurons could intersect, or they could bundle together; occasionally, closely clustered somas were also observed. Using the DAPI signal, neurons that exhibited interactions with background objects or unspecified cells were excluded from the dataset unless they met specific criteria. These conditions stipulated that a single neuron must occupy a minimum of 10,000 pixels and contain precisely one nucleus. Furthermore, the pixel area of its nucleus had to fall within the range of 200 to 3,000, and the circularity of neurons had to be less than 0.25. Circularity in this study is defined as $C = 4 * \pi * A/P^2$, where A and P are the area and parameter of the extracted neuron shape, respectively.

Care was taken to ensure the isolated neurons were appropriate for automated neuronal tracing, as the quality of the reconstructed neurons is directly linked to the quality of the extracted neuron images. Apart from touching neurons, there were other issues associated with the isolated neurons that could affect the subsequent neuronal tracing. For example, the neurites from the same neuron could form 'loops' by interfering with themselves. Neurons exhibiting this kind of morphology posed challenges for accurate tracing, primarily stemming from difficulties in pinpointing the intersection points. Some early-developing neurons also had a large growth cone located at the terminal end of the nascent axon. Unlike the nearly cylindrical neurites, the thickness generally varies across the thin growth cone and its precise morphology cannot be determined without the use of more advanced 3D fluorescence microscopy. Because the images of the neuronal cultures were collected using an automated scanning system, there was less control over the image acquisition process. Subsequently, some regions on the coverslip were out of focus and appeared blurry. Neuronal tracing from these blurry images would lead to neurons with incorrect 3D reconstruction. To address this issue, we define an image quality metric that quantifies the sharpness of images as follows: for an image I of size $m * n$, let $F[I]$ be the centered Fourier transform of the image I, and F_M denote the magnitude spectrum of $F[I]$. We choose a threshold value of $T = max(F_M)/1000$ and compute the total number of pixels in F_M whose pixel values are greater than the threshold T, denoted as S_H (number of high-frequency components). The image blurriness is then calculated by the equation $B = S_H/(m * n)$.

To properly handle the issues discussed above, a hierarchy of filters was set to ensure the quality of the final isolated neurons: neurons containing loops were identified using the 'regionprops' function; neurons with a large growth cone were determined by applying the Euclidean distance transform ('bwdist' function) to the binary image of the extracted neuron shape, and then checking whether it contained a local maximum with a value comparable to that of the soma in the transformed domain; isolated neuron images were classified as 'blurry' if their blurriness value is less than 0.02. The neuron images that met any of the conditions above were removed from the subsequent analysis, while unhindered, clear isolated neuron images were output into separate tiff files. After generating the output images, a manual inspection was conducted to ensure their quality.

Semi-automated neuronal tracing

Neuronal tracing of individual neurons from the output tubulin images was carried out through the all-path-pruning 2.0 (APP2) algorithm.[69] The algorithm consists of three steps: in the first step, the gray-weighted distance transform (GWDT) of the input image is computed, and the soma is detected by finding the position with the maximum distance-transformed value; a fast-marching-based algorithm then uses this estimated soma position as the seed to construct an initial, over-reconstruction of the traced neuron; this initial reconstruction is followed by a hierarchical pruning process to remove the redundant segments, which produces a final succinct representation of the neuron. In this work, the following parameters were used for the APP2 algorithm: GWDT, auto-background thresholding, and resampling of the neuronal skeleton were enabled whereas downsampling and gap joining were disabled, and the threshold for the minimal segment length was set to 3 pixels (~1 μm). The individual neuron images were batch processed by implementing the Vaa3D APP2 plugin[68] from the MATLAB interface, and the morphological data of the final reconstruction were stored in SWC format. The output SWC files were inspected, and any files that did not yield desirable reconstructions were re-traced by fine-tuning the threshold parameters.

Neuron model and computation of the lowest order harmonic

Neuron shape embedded in the SWC format is defined by a set of points $\{\boldsymbol{s}_i = (i, x_i, y_i, z_i, r_i, j) | i, j \in \{1, 2, \ldots, M\}; x_i, y_i, z_i, r_i \in \mathbb{R}; i < j\}$ in the 6-dimensional space, where each point $\boldsymbol{s}_i$ is a sphere with center (x_i, y_i, z_i) and radius r_i. Here, M is the total number of skeletal points contained in the SWC file and $\boldsymbol{s}_0$ is the fictitious point defining the root of the neuronal tree. There is only one parent point $\boldsymbol{s}_j$ associated with each point $\boldsymbol{s}_i$ to avoid the formation of loops. In this way, each pair of adjacent points define a unique conical frustum-shaped segment, in which the upper and lower base radii of the frustum are given by the radius at the corresponding skeletal points. For ease of mathematical formulation, the neuron model is compartmentalized such that each skeletal point defines the center of a unique compartment approximated as the union of the closest half-frustums formed with the centers of its adjacent compartments (half-frustums defined by the domains enclosed by the surface of the conical frustum and the bisecting plane of the line segment connecting the two points), a schematic of this compartmentalization is shown in Figure S6A. In this way, we avoid introducing new points to the system and dealing with the flux at the branching points. Given a compartment i and one of its adjacent compartments j, let V_i, d_{ij} and A_{ij} denote the volume of compartment i, the Euclidean distance between the two centers of the two compartments and the area of the circular boundary between the two compartments. We show that the eigenfunctions of the Laplace-Beltrami operator with the homogeneous Neumann boundary condition can be approximated by the corresponding eigenvectors of a negative Laplacian matrix L that encodes geometric information of the neuronal shape (see SI for the derivation and validation):

$$L_{ij} = \begin{cases} \sum_{k\sim i} \frac{A_{ik}}{V_i d_{ik}}, \text{if } i = j, \{i,k\} \text{ connected} \\ -\frac{A_{ij}}{V_i d_{ij}}, \text{if } i \sim j, \{i,j\} \text{ connected} \\ 0 \quad \text{otherwise} \end{cases} \qquad \text{(Equation 1)}$$

Note that the homogeneous Neumann boundary conditions at the terminal points of axon and dendrites were implemented via the standard ghost point method. The Laplacian matrices were constructed in MATLAB. The lowest order spatial harmonic was evaluated at the skeletal points using the 'eig' function. Subsequently, the nodal plane was determined by performing linear interpolation of the lowest order harmonic along the edges of the mesh/skeleton and determining the position of the zero-crossing point along the skeletal/mesh edges. This discrete Laplacian approach was validated by comparing the lowest order harmonics with those calculated using the finite element method on a three-dimensional volumetric neuron mesh (see Figure S6 for details).

Analysis of AnkG cluster

For ease of analysis, the intensity of labeled AnkG was first estimated at the skeletal points from the fluorescence images. Due to the limited pixel resolution of the neuronal image, the skeletal points were not always perfectly aligned to the center of the neurites. Besides, there were additional fluctuations in intensity across the width of the neurites. For these reasons, a direct mapping of pixel intensities at the skeletal points may not be suitable as it could induce extra noise and further complicate the results. To minimize these effects, the following procedure was used: the pixel intensities were evaluated along the line segment perpendicular to the skeletal segments, this signal was then smoothed by fitting with a Gaussian function, and the intensity at the skeletal point was estimated as the peak value of the fitted curve. The averaged

peak value was used in the case where there were multiple skeletal segments associated with a single skeletal point (e.g., bifurcation points like soma and branch points).

To detect the location of the AnkG peak along the nascent axon, the AnkG signal along the nascent axon was smoothed using a moving average filter with a window size of 3–8 μm (depending on the noise level of the signal) and the region of the major AnkG peak of interest was fitted with a shifted lognormal function of the form

$$I_{\mathrm{AnkG}}(x) = \frac{a}{x} exp\left(- \frac{ln(x) - \mu^2}{2\sigma^2} \right) + b, \quad \text{(Equation 2)}$$

using the least squares method. Where x is the path distance to the soma center and the parameters $\{a, b, \mu, \sigma\}$ are all determined from the fit. The peak location was calculated as $exp(\mu - \sigma^2)$, and the height of the peak is given by the height of the lognormal function without the vertical shift, i.e., $h_p = a \cdot exp(\sigma^2/2 - \mu)$. The length of the AnkG-rich region is defined as the full width at quarter maximum (FWQM) of the unshifted lognormal function, where the boundaries of the region are given by

$$x = exp\left(\mu - \sigma^2 \pm \sqrt{2\sigma^2 \, ln\, 4}\right). \quad \text{(Equation 3)}$$

We defined that an AnkG peak must have a peak height of 100 pixel value (intensity) and a width of greater than 10 μm to be included in our data processing.

Derivation of the discrete laplacian

In spite of the high accuracy achieved by computing Laplace-Beltrami eigenfunctions using the finite element method (FEM), its suitability for high-throughput analysis involving a large number of neurons is limited. This limitation primarily arises from the considerable challenge of generating high-quality, watertight neuronal meshes from SWC files. The intricate geometry of neurons often results in volumetric meshes that are difficult to handle on standard personal computers due to limited memory. Additionally, existing neuronal mesh generation tools typically demand substantial manual effort for mesh repair and refinement prior to use, which makes the process extremely time-consuming. To address these computational limitations, we developed an alternative approach where the Laplace-Beltrami operator was approximated using a discrete Laplacian operating on the skeletal points of the neuronal structure. Although this approximation resulted in reduced accuracy of the eigenspectra and associated eigenfunctions, it significantly alleviated the computational effort required for their computation. In the following section, we provide a detailed derivation of this discrete Laplacian based on the connected conical-frustum representation of the neuron (see Figure S6A).

Considering a compartment defined by the bounded domain Ω_i, with its center $\boldsymbol{s}_i$ and one of its adjacent compartments Ω_j with center $\boldsymbol{s}_j$, we denote the circular cross-section of the frustum connecting Ω_i and Ω_j, oriented parallel to its bases and positioned at the middle of the long axis, as $\partial\Omega_{ij}$. The area of this circular cross-section is denoted as A_{ij}, which is the same as A_{ji}. Recall that the bounded domain Ω_i is defined the union of half-frustums formed with its adjacent centers. Assume there are N compartments adjacent to Ω_i, and the corresponding circular cross-sections between these compartments are denoted by $\{\partial\Omega_{i1}, \partial\Omega_{i2} \ldots, \partial\Omega_{iN}\}$, with respective areas $\{A_{i1}, A_{i2} \ldots, A_{iN}\}$, and outward pointing unit normal vectors $\{\boldsymbol{n}_{i1}, \boldsymbol{n}_{i2}, \cdots, \boldsymbol{n}_{iN}\}$. It is important to note that these cross-sections are not physical membranes but rather part of the intracellular space, allowing particles to freely diffuse across them. Conversely, the homogeneous Neumann boundary condition is applied to the lateral surface, representing the impermeable plasma membrane of the neuron. We denote this lateral surface as $\partial\Omega_{lat,i}$, with the outward pointing unit normal vector $\boldsymbol{n}_{lat,j}$. By considering the integral form of the diffusion equation in a particular compartment Ω_i, we have the following equation:

$$\int_{\Omega_i} \partial_t u_i dV = D_i \sum_{j=1}^{N} \left(\int_{\partial\Omega_{ij}} \nabla_{\boldsymbol{n}_{ij}} u \big|_{\partial\Omega_{ij}} ds + \int_{\partial\Omega_{lat,j}} \nabla_{\boldsymbol{n}_{lat,j}} u \, ds \right), \quad \text{(Equation 4)}$$

where ∂_t is the partial derivative with respect to time t, and $\nabla_{\boldsymbol{n}} u = \nabla u \cdot \boldsymbol{n}$ is the directional derivative describing the rate at which u changes in the direction $\boldsymbol{n}$. Under the assumptions of the homogeneous concentration in the perpendicular plane along the long axis of the conical frustum, and the constant diffusion constant D in all compartments, the second integral on the right-hand side of the equation vanishes and we obtain:

$$\int_{\Omega_i} \partial_t u_i dV = D \sum_{j=1}^{N} A_{ij} \nabla_{\boldsymbol{n}_{ij}} u \big|_{\partial\Omega_{ij}}. \quad \text{(Equation 5)}$$

To further simplify the equation, we approximate the mean particle concentration $\overline{u}_i$ in Ω_i as

$$\overline{u}_i = \frac{1}{V_i} \int_{\Omega_i} u_i dV, \quad \text{(Equation 6)}$$

and approximate the boundary flux across the surface $\partial\Omega_{ij}$ as

$$\nabla_{n_{ij}} u\big|_{\partial\Omega_{ij}} = \frac{\overline{u}_j - \overline{u}_i}{d_{ij}}, \quad \text{(Equation 7)}$$

where V_i is the total volume of Ω_i, and $d_{ij} = \|s_j - s_i\|$ is the Euclidean distance between the centers of the two compartments. Assume that u_i is well-behaved that we can reverse the order of integration. Using Equations 5, 6, and 7 simplifies to

$$\partial_t \overline{u}_i = \frac{D}{V_i} \sum_{j=1}^{N} \frac{A_{ij}}{d_{ij}} \left(\overline{u}_j - \overline{u}_i\right). \quad \text{(Equation 8)}$$

Suppose that the neuron is described by a total of M compartments, the system of Equation 4 for the multi-compartmental neuron model can be written in matrix form as

$$\partial_t \boldsymbol{u} = -DL\boldsymbol{u}, \quad \text{(Equation 9)}$$

where $\boldsymbol{u} = (\overline{u}_1, \overline{u}_2, \ldots, \overline{u}_M)$ is the column vector of the morphogen concentrations at the corresponding compartment and L is the discrete Laplacian matrix given by

$$L_{ij} = \begin{cases} \sum_{k\sim i} \frac{A_{ik}}{V_i d_{ik}}, \text{if } i = j, \{i,k\} \text{ connected} \\ -\frac{A_{ij}}{V_i d_{ij}}, \text{if } i \sim j, \{i,j\} \text{ connected} \\ 0 \quad \text{otherwise} \end{cases} \quad \text{(Equation 10)}$$

Numerical validation of the discrete laplacian approach

For the purpose of validation, a comparison was conducted between the lowest order spatial harmonics obtained using the discrete Laplacian approach and the standard FEM for cultured neurons. In the discrete Laplacian approach, the Laplacian matrix was constructed using MATLAB 2016b (MathWorks), and the lowest order harmonic was computed at the skeletal points using the 'eig' function. For the FEM, the computation of the spatial harmonic involved several steps. Firstly, the traced neuronal structure was scaled up by a factor of 10, and a triangle surface mesh was generated using the 'marching cubes' algorithm.[70] Subsequently, 10 iterations of tangential smoothing and 30 iterations of geometric smoothing were performed using 'shapeDNA'.[71] The resulting surface mesh was then simplified to 50k vertices using quadric error metrics[72] and repaired using Nettfab (Autodesk Fusion 360 V.2.0.12392). Finally, a tetrahedral volume mesh was created using Gmsh 4.9.5[73] based on the surface mesh, followed by refinement using the Optimize 3D and Optimize 3D(Netgen) functions. In Figure S6C, we compare the lowest order harmonics solved using both the FEM (top-left) and the discrete Laplacian approach (top-right). The sign diagrams reveal a slight shift of the nodal plane position toward the soma (~5 μm) in the discrete Laplacian solution compared to the FEM solution. However, the solutions exhibit overall qualitative similarity. Figure S6D further emphasizes the similarity between the FEM solution (blue) and the discrete Laplacian solution (orange) as the solutions are projected onto the Y axis. This provides further validation for the effectiveness of our discrete Laplacian approach.

Impact of soma shape on nodal plane position

While constructing the discrete Laplacian to evaluate the lowest order harmonics, the digitally traced neurons are compartmentalized with the soma compartment treated as a solid sphere. However, this simplification raises concerns about the accuracy of the model since the actual volume of the soma compartment depends on the deformation of the membrane in that region. Moreover, the impermeability of the nucleus within the soma to certain proteins or molecules, particularly those with a molecular mass greater than approximately 50kDa,[74,75] further complicates the model. As this would mean that a fraction of the intracellular space in the soma is occupied, resulting in a reduced compartmental volume and distorted diffusive path within the soma.

Proper modeling of these effects would require a three-dimensional characterization of neuronal morphology, which is currently unavailable. To provide a coarse-grained estimation of the uncertainties associated with the position of the nodal plane, we investigated how the nodal plane position changes relative to its original position when the volume of the soma compartment (V_{soma}) is increased or decreased by 20%. The resulting shifts of the nodal plane are depicted in the histogram (Figure S7A). We found that a decrease in soma volume causes the nodal plane to shift toward the distal axon (red), while an increase in soma volume leads to a shift in the opposite direction toward the soma (violet). Most of the absolute shifts of the nodal plane are less than 5 μm, which are negligible compared to the overall size of the neuron (within 2% of the neuronal path length, see Figure S7B). Consequently, although the morphology around the soma is not accurately modeled, it does not significantly affect the calculation of the spatial harmonics. Therefore, we believe that the position of the nodal plane is reasonably estimated.

QUANTIFICATION AND STATISTICAL ANALYSIS

No statistical analysis is used.